Skin capillary endothelial cells form a network of spatiotemporally conserved Ca^{2+} activity

Anush Swaminathan[1], David G. Gonzalez[1], Catherine Matte-Martone[1], Fei Xu[1], Deandra Simpson[1], David Monedero-Alonso[1], Jessica L. Moore[1], Julia J. Mack[*2,3], Chen Yuan Kam[*4,5], Valentina Greco[*1,6,7]

Affiliations

[1]Department of Genetics, Yale School of Medicine, New Haven, CT 06510, USA
[2]Department of Medicine, Division of Cardiology, UCLA, Los Angeles, CA 90095, USA
[3]Molecular Biology Institute, UCLA, Los Angeles, CA 90095, USA
[4]Department of Medicine, Division of Dermatology, UCLA, Los Angeles, CA 90095, USA
[5]Broad Stem Cell Research Center, UCLA, Los Angeles, CA 90095, USA
[6]Departments of Cell Biology and Dermatology, Yale Stem Cell Center, Yale Cancer Center, Yale School of Medicine, New Haven, CT 06510, USA
[7]Howard Hughes Medical Institute (HHMI), Chevy Chase, MD, USA

*Co-correspondence to: Valentina Greco, valentina.greco@yale.edu, Chen Yuan Kam chenyuankam@mednet.ucla.edu, Julia J. Mack, jmack@mednet.ucla.edu

Abstract

Ca^{2+} signaling and its regulation are important for endothelial cell (EC) functions, including local blood flow control, mechanotransduction, and barrier function. Yet the spatiotemporal organization of Ca^{2+} activity and its regulation across a vascular plexus is poorly understood in an *in vivo* mammalian context, largely due to technical barriers. To overcome this gap in knowledge, we developed an approach to resolve Ca^{2+} activity with single cell resolution in the skin vasculature of live adult mice by multi-photon imaging. Here, we tracked thousands of Ca^{2+} events in the skin capillary plexus during homeostasis and observed signaling heterogeneity between ECs, with just over half displaying Ca^{2+} activity over minutes. Longitudinal tracking of the same mice revealed that the same ECs maintain Ca^{2+} activity over days to weeks. Interestingly, activity dynamics, such as frequency and event duration, are not conserved at a single cell level but at an EC population level. To identify the molecular underpinning of this spatiotemporal Ca^{2+} activity, we conditionally deleted in ECs the most expressed gap junction protein - Connexin 43 (Cx43). We found that loss of Cx43 initially causes a subset of ECs to display sustained Ca^{2+} activity and biases the dynamics of the whole network towards chronically persistent activity over time. Lastly, through pharmacological targeting of a small panel of known Ca^{2+} mediators, we showed that inhibition of L-type Voltage Gated Ca^{2+} channels largely restores physiological Ca^{2+} activity after loss of Cx43, but has no effect on signaling dynamics in homeostatic settings.

Significance Statement

Ca^{2+} signaling in mammalian endothelial cells (ECs) locally regulates blood flow, force sensing, and vessel permeability. In periods of vascular development and repair, there is a need for large-scale coordination in each of those functions. To understand what mechanisms drive collective Ca^{2+} activity during vascular remodeling, we must first address the open question of how tissue-level Ca^{2+} is spatiotemporally organized and regulated during homeostasis. Intravital imaging in skin vasculature of live mice reveals that a conserved set of cells orchestrates tissue-wide Ca^{2+} from minutes to days to weeks. How this network maintains itself over time requires long-range communication through a gap junction protein, Connexin 43 (Cx43). Cx43 dysregulation subsequently recruits L-type Voltage Gated Ca^{2+} channels to reshape the EC Ca^{2+} landscape.

Introduction

Ca^{2+} is an essential second messenger, mediating tightly regulated signaling pathways to integrate spatial and temporal information across multiple scales, from individual cell transients to multi-cell patterns (1-5). *In vitro*, the temporal dynamics of Ca^{2+} activity within cells differentially encodes downstream functions, enabling its versatility as a signaling pathway (6-11). In excitable tissues *in vivo*, such as basal and lateral amygdala (BLA) after application of a conditioning stimuli, there is considerable overlap in which specific neurons are active over days (12). Moreover, the BLA network displays tightly conserved population-level properties, such as maintenance of total proportion of Ca^{2+} active neurons over time (12). In non-excitable tissues *in vivo*, we demonstrated that cells in the epidermal stem cell compartment engage in both local and large-scale Ca^{2+} activity without any stimuli (4). These tissue-wide analyses revealed that all epidermal stem cells display Ca^{2+} activity within one day during homeostasis. However, *in vivo* Ca^{2+} activity, characteristics, and regulation, across other tissues, especially in mammalian systems, remains relatively unexplored.

Endothelial cells (ECs) are specialized squamous cells that line the lumen of all blood vessels (13). The endothelium regulates key functions in the vasculature through Ca^{2+} activity, such as angiogenesis, vessel tone, local blood flow control, mechanotransduction, and barrier integrity (14-19). *In vivo* work in zebrafish vasculature during development has tracked Ca^{2+} across EC populations and identified spatiotemporally organized Ca^{2+} activity specifically in cells driving vessel remodeling (tip cells) (20). These cells also display variable Ca^{2+} temporal dynamics which shape downstream vessel fates (20). Recently, more studies have focused on mouse brain capillaries -given their role in the exchange of gases, nutrients and metabolic waste- to identify molecular mechanisms driving Ca^{2+} signaling within individual ECs, including IP_3R-mediated Ca^{2+} release, and how channels including Kir2.1, TRPV4, TRPA1, and Piezo1 shape Ca^{2+} influx (21-25). Yet, there are major gaps in our understanding of Ca^{2+} organization and temporal dynamics during homeostasis across an entire mammalian vascular plexus in the native, unperturbed tissue environment.

Organization of Ca^{2+} activity also involves information exchange between cells, as ECs can coordinate Ca^{2+} activity in response to different homeostatic cues (26-30). While individual ECs can regulate cytoplasmic Ca^{2+} concentrations through a variety of mechanisms, multicellular coordination of Ca^{2+} activity between ECs has largely been studied in the context of gap junction-mediated intercellular communication (31). Gap junctions are intercellular channels that allow for cell-cell communication in all tissues, including the vasculature, through electrical coupling and transfer of second messengers such as IP_3 (32, 33). Evidence for EC coordination during homeostasis, development and injury indicates that molecular signaling may not only be influenced by direct neighbors but regulated on a tissue-wide scale (34-38). Gap junctions have recently been implicated in coordination of Ca^{2+} signaling networks in other tissues such as epithelial stem cells and blood progenitor stem cells. Loss of Connexin 43 (Cx43) gap junctions leads to tissue-wide uncoupling of coordination across the epidermal stem cell compartment and repeated, more frequent, and longer signaling within restricted neighborhoods (4). In *Drosophila* lymph glands, perturbing pan-gap junctions changes the Ca^{2+} signaling frequency and promotes precocious differentiation of blood progenitors (39).

Despite these important insights, it remains challenging to study Ca^{2+} dynamics in an *in vivo* mammalian system given the technical challenges of tracking ECs and their signaling across space and time. Here, we overcome this challenge by focusing on the skin capillary plexus - due to its critical roles in nutrient and oxygen delivery - and tracking Ca^{2+} dynamics in hundreds of ECs over time through our non-invasive, intravital imaging approach (Figure S1) (4, 36). We observed extensive Ca^{2+} activity across capillary plexus ECs during homeostasis, with patterns of Ca^{2+} conserved spatially within the same cells and temporally at the network level. To probe how the spatiotemporal organization of EC Ca^{2+} activity is coordinated, we conditionally deleted Connexin 43 (Cx43cKO) in ECs, and discovered chronically sustained Ca^{2+} activity and dysregulation of EC temporal coordination across the capillary plexus. Finally, we show that L-type Voltage Gated Ca^{2+} channels (VGCCs) are responsible for aberrant Ca^{2+} entry specifically after Cx43cKO, unlike in the wildtype setting. Altogether, this study defines the spatiotemporal organization and regulation of Ca^{2+} activity by a conserved EC network in the skin capillary plexus.

Results

Spatiotemporal analyses of the skin capillary plexus reveal a network of endothelial cells with conserved Ca^{2+} activity over time.

Understanding plexus-wide Ca^{2+} activity is fundamental to reveal how ECs coordinate their signaling to achieve proper vascular function. The superficial nature of the skin capillary plexus makes it especially tractable to longitudinal tracking of an *in vivo* EC population through non-invasive multi-photon microscopy. Here, we aimed to gain a plexus-wide view of Ca^{2+} activity in skin capillaries with single-cell resolution. Towards this goal, we recorded Ca^{2+} activity with simultaneous imaging of Ca^{2+} dynamics and EC nuclei via genetically encoded fluorescent

reporters. We used an EC-specific inducible Cre driver under the control of the vascular endothelial cadherin (VECad) promoter to simultaneously recombine a nuclear H2B-mCherry reporter and GCaMP6s, a Ca^{2+} reporter encoding a calmodulin-GFP fusion protein (VECadCreER; GCaMP6s; H2B-mCherry) (Figure S1 A). We focused on a simplified skin model devoid of hair follicles - palmoplantar skin - and recorded Ca^{2+} activity in the capillary plexus (4 to 5 regions per mouse with 75-150 cells in each region) over a period of 17 minutes and 12 seconds (300 frames at 3.44s/frame) in adult (2-4 months old) anesthetized mice via two-photon microscopy. During these timelapse recordings, we observed dynamic and heterogeneous Ca^{2+} activity across the plexus with hundreds of events per region and different levels of Ca^{2+} activity and dynamics between cells (Figure 1 A; Movie 1). To quantitatively analyze the dynamics of the observed Ca^{2+} activity, we devised a computational analysis pipeline that segments individual ECs by using the position of the nuclear H2B-mCherry signal as a proxy for the cell body (Figure S1 A). This enabled us to isolate and analyze changes in GCaMP intensity of each individual cell within the imaging region for the entire duration of the timelapse recording (Figure S1 B e-g). The pipeline determines the number and duration of Ca^{2+} events per cell without being confounded by variable baseline Ca^{2+} levels, through counting any activity above a set threshold as an event (>50% change in average MFI above the minimum MFI) (Figure S1 B; Figure 1 A). We analyzed 1,765 cells across 4 mice and discovered that just over half of ECs (52.4 ± 7.34%) exhibited Ca^{2+} activity during the timeframe of recording (defined as having an 'active' cell status, with the others assigned a status of 'inactive'; Figure 1 B). Using our pipeline, we found that the majority of active ECs display dynamics within a defined range in both frequency (0.445 ± 0.440 events per minute, encompassing 83.9 ± 7.50% of cells) and average duration (8.36 ± 8.15 seconds per event, encompassing 91.3 ± 3.84% of cells) of Ca^{2+} events (Figure 1 C). A small population of ECs displayed activity above that range, showcasing either high frequency (1.31 ± .351 events/minute) or high average duration (29.8 ± 16.4 seconds per event) dynamics (Figure 1 C; Figure S2 A). Lastly, to understand the prevalence of multi-cellular activity, we adapted our pipeline to identify neighboring cells displaying Ca^{2+} activity either within the same time frame or one frame apart, and calculated the number of cells involved (Figure 1 D; Figure S1 A and B a-d). We found that the most represented cluster size for EC Ca^{2+} activity occurred across 2-4 cells (42.8 ± 5.64% of total activity) with a small percentage involving 5 or more cells (2.97 ± 1.32% of total activity) (Figure 1 E).

As we established a quantitative understanding of EC Ca^{2+} dynamics, we next asked how activity status is regulated over longer periods of time. Towards this goal, we leveraged our longitudinal imaging approach that allows us to revisit the same cells over days to weeks. We began with short-term revisits and intriguingly, discovered that not only was the proportion of active and inactive cells largely conserved after 24 hours (58.7 ±14.4% active on Day 0 vs. 52.0 ± 18.8% on Day 1), but activity status was also conserved at the cellular level (71.1 ± 6.03% of cells maintained their activity status after 24 hours) (Figures 1 F and G; Figure S2 B; Movie 2). We also observed that only 28.9 ± 7.89% of high frequency and 17.0 ± 6.30% of high average duration ECs retained their dynamics after 24 hours, indicating that despite maintaining activity status

(active vs. inactive), individual ECs largely exhibit different Ca^{2+} dynamics (frequency and average duration) over days (Figure 1 H and I; Figure S2 C).

Next, we asked whether Ca^{2+} activity status is also conserved over a longer time frame. Given our past work demonstrating that ECs remain positionally stable over weeks in adults (36), we revisited the same regions 2 weeks later (Figure S3 A). Strikingly, we observed that a majority (67.8 ± 7.56%) of the same ECs retained their activity status (Figure 1 J-K; Movie 3) even though their dynamic properties were largely not retained (5.58 ± 6.51% retention of high frequency ECs and 0% retention of high average duration ECs) (Figure 1 L). Interestingly, we found that Ca^{2+} dynamics (frequency and average duration), though not conserved at the cellular level, were maintained over weeks at the network level (Figure 1 L-O). Lastly, the proportion of Ca^{2+} activity involving EC clusters was also conserved over weeks (Figure 1 P).

Collectively, our findings demonstrate that Ca^{2+} activity in the skin capillary plexus is dynamic during vascular homeostasis and spatially patterned by an active network of ECs with temporally conserved properties over weeks.

Loss of endothelial Connexin 43 leads to chronically sustained Ca^{2+} activity impairing long-term network regulation

Our findings that EC Ca^{2+} properties are conserved at the network level over time raise the question of how this is regulated molecularly. Gap junctions are intercellular channels that have established roles in EC communication and functional coupling (40-42). We hypothesized that maintenance of the active network is spatially coordinated by gap junctions. Connexin 43 is a gap junction protein both widely expressed in the vasculature, and the most expressed Connexin isoform in isolated skin ECs (Figure S3 B i) (43, 44). To investigate the role of Cx43 in the regulation of network Ca^{2+} activity, we combined our Ca^{2+} reporter with Cx43 knockout mice ($Cx43^{fl/fl}$) to generate EC conditional knockouts (VECadCreER; GCaMP6s; H2B-mCherry; $Cx43^{fl/fl}$) and compared them to littermate controls (VECadCreER; GCaMP6s; H2B-mCherry; $Cx43^{+/+}$).

Cx43cKO and control mice were induced over 4 consecutive days (2mg Tamoxifen daily) and then imaged 3 days later (1 week following the first Tamoxifen injection – referred to as Day 0). Surprisingly, we observed an increase in capillary plexus Ca^{2+} activity in Cx43cKO mice compared to wildtype controls (Figures 2 A-B; Movie 4). This included a significant increase in the proportion of active ECs (68.6 ± 3.71% in Cx43cKO mice vs. 50.8 ± 8.47% in control mice) (Figure 2 C). We also observed that the active network in Cx43cKO mice displayed significantly increased frequency (0.646 ± 0.586 events/min in the Cx43cKO mice vs. 0.473 ± 0.467 events/min in control mice) and a striking ~7-fold increase in the average duration of Ca^{2+} events (62.5 ± 119s in the Cx43cKO mice vs. 8.00 ± 7.33s in control mice) (Figures 2 D-E). Furthermore, we found a group of ECs which displayed significantly long-lasting Ca^{2+} events ranging between 2 and 17

mins, a behavior of persistent activity not detected in control mice (19.3 ± 6.51% of active ECs in Cx43cKO mice vs. 0.324 ± 0.305% of active ECs in control mice) (Figure 2 F).

In contrast to control mice where EC clusters were active simultaneously only for a few frames, Cx43cKO showed "persistently active" EC clusters (61.7 ± 17.3% involved at least 2 cells), simultaneously active for the entire duration of recording (Figure S3 C-E). To understand whether changes in expression of other vascular Connexins (41) may influence Ca^{2+} activity in Cx43cKO mice, we used qPCR to analyze Connexins 37 and 40 expression in isolated skin ECs and found their transcripts to be similarly expressed in Cx43cKO versus control samples, indicating absence of compensatory changes in expression (Figure S3 B ii).

We next asked whether spatiotemporal Ca^{2+} activity and network-level dynamics of ECs is conserved over time in Cx43cKO mice, as was observed under physiological conditions. Revisiting the same cells in the same Cx43cKO mice, we found that the activity status of ECs was spatially conserved on a single cell level after 14 days (78.4 ± 4.84% of ECs retained their status) (Figure S3 F). Furthermore, persistent Ca^{2+} activity was also conserved on a cellular level after 14 days (78.9 ± 11.5% of persistently active ECs on Day 0 retained their behavior on Day 14) (Figures 2 G-J and L; Movie 5). While there was no change in the proportion of active Cx43cKO ECs after 14 days (Figure 2 N), we observed an increase in the proportion of persistently active cells (32.2 ± 22.9% on Day 0 vs. 57.3 ± 12.2% of active ECs on Day 14) (Figures 2 K and M; Movie 5). This was accompanied by an increase in the cluster size of ECs with persistent activity (from 3.85 ± 4 cells on Day 0 to 6.73 ± 7.99 cells on Day 14) (Figure 2 O). While control mice demonstrated conserved dynamics across the network after 14 days, Cx43cKO mice showed a significant increase in average duration (123 ± 156s on Day 0 vs. 194 ± 165 s on Day 14) and a significant decrease in frequency (0.445 ± 0.432 events/min on Day 0 vs. 0.319 ± 0.322 events/min on Day 14), consistent with the observed increase in the number of persistently active cells (Figures 2 P and Q).

Our findings show that loss of Cx43 increases plexus-wide Ca^{2+} activity and enriches for a population of persistently active ECs. In addition, we found that loss of Cx43 maintains spatial patterning over weeks, but biases ECs towards longer-lasting Ca^{2+} activity, and accordingly, persistently active ECs become a larger fraction of the vascular plexus over time.

L-type Ca^{2+} channels sustain elevated Ca^{2+} dynamics following loss of endothelial Connexin 43

Our findings revealed an unexpected increase in Ca^{2+} activity across the EC network after loss of Cx43. To identify what molecular mediators are responsible for this signaling phenotype, we tested a small drug panel of well-known inhibitors of ion channels involved in Ca^{2+} entry. Specifically, we topically applied GSK219 (TRPV4 inhibitor), Dooku1 (Piezo1 inhibitor), Nifedipine (L-type Ca^{2+} channel inhibitor), and DMSO vehicle in Cx43cKO mice and imaged the

same capillary regions before and after treatment (within 30-60 minutes) (17, 45, 46). Interestingly, we observed that nifedipine appeared to largely decrease total Ca^{2+} activity and persistent activity in Cx43cKO mice relative to the other compounds (Figure S4).

Nifedipine is a well-established inhibitor of voltage gated L-type Ca^{2+} channels, blocking Ca^{2+} influx as a response to membrane potential changes (46-49). To first test whether nifedipine would alter Ca^{2+} activity in capillary ECs during homeostasis, we used wildtype (VECadCreER; GCaMP6s; H2B-mCherry) mice and compared the proportion of active ECs, as well as mean values of frequency and average duration by cell per mouse, before and after treatment with nifedipine or DMSO. We did not observe a significant difference in proportion of active ECs (13.7% ± 18.2% decrease after nifedipine treatment vs. 20.2% ± 15.0% decrease after DMSO treatment), frequency (20.6% ± 20.5% decrease after nifedipine treatment vs. 17.8% ± 17.9% decrease after DMSO treatment), or average duration (3.08% ± 8.73% decrease after nifedipine treatment vs. 11.8% ± 7.47 % decrease after DMSO treatment) (Figures 3 A-C and E; Movie 6). In addition, distributions of Ca^{2+} event frequency and average duration by cell were also not significantly different before and after nifedipine treatment, suggesting that L-type channel inhibition does not affect network-wide Ca^{2+} activity in wildtype mice (Figures 3 D and F).

Next, to probe deeper into the effect of nifedipine treatment on Ca^{2+} activity in Cx43cKO mice, we repeated the experiments in Figure S4 utilizing the H2B-mCherry nuclear reporter necessary for single EC segmentation and quantitative analyses. Compared to control DMSO treatment, nifedipine treatment led to decreased proportion of active ECs (39.0% ± 12.6% decrease after nifedipine treatment vs. 6.29% ± 6.23% decrease after DMSO treatment), frequency (21.5% ± 18.5% decrease after nifedipine treatment vs. a 20.0% ± 21.5% increase after DMSO treatment), and average duration (72.8% ± 37.0% decrease after nifedipine treatment vs. 29.3% ± 11% decrease after DMSO treatment) (Figures 3 G-I and K; Movie 7). In addition, the distributions of Ca^{2+} event frequency and duration were decreased after nifedipine treatment compared to before treatment (Figures 3 J and L). We next analyzed the effects of nifedipine on persistently active cells in Cx43cKO mice and confirmed a decrease in persistent activity after treatment (19.9% ± 9.3% of persistently active cells retained after nifedipine treatment vs. 62.9% ± 2.65% after DMSO treatment) and an accompanying decrease in mean cluster size of persistently active ECs (50.5% ± 9.53% decrease after nifedipine treatment vs. 18.4% ± 14.0% decrease after DMSO treatment) (Figures 3 M-Q).

These data show that L-type Ca^{2+} channels mediate elevated and persistent EC Ca^{2+} activity after loss of Cx43 (Figure 4). In contrast, these channels do not seem to influence EC Ca^{2+} dynamics in wildtype mice during homeostasis.

Discussion

How Ca^{2+} activity is organized, maintained, and regulated across a mammalian vascular plexus in its native, unperturbed tissue environment has been poorly understood. To our knowledge, our study represents the first time that Ca^{2+} activity of an *in vivo* population of mammalian ECs has been longitudinally tracked over minutes to days to weeks, demonstrating unexpected spatiotemporal patterns of Ca^{2+} activity and dynamics. Our tissue-wide analysis reveals a network of active cells conserved over time, orchestrating Ca^{2+} activity (Figure 4). Coordinated Ca^{2+} activity as a baseline in adult capillary homeostasis highlights that organized cell networks control Ca^{2+} activity at the tissue-level, and reinforces the notion of the endothelium being a functional syncytium (29, 42, 50). Critically, we discovered that Cx43 functions to constrain Ca^{2+} activity within a dynamic range and maintain network signaling dynamics over the long-term (Figure 4). Our findings elucidate a role of Cx43 as a mediator of cell-cell communication on a larger, tissue-wide scale than previously reported, and as a regulator of temporal coordination of the conserved skin EC network. Furthermore, we found that L-type VGCCs contribute to persistent Ca^{2+} activity after Cx43 loss, uncovering a novel interplay between aberrant L-type VGCC activity and Cx43 dysregulation (Figure 4).

In this study, we discovered and quantified the organization and regulation of homeostatic Ca^{2+} activity in skin vasculature through our unique ability to resolve tissue-wide Ca^{2+} dynamics with single cell resolution *in an intact, uninjured mouse*. The widespread Ca^{2+} activity in skin endothelial cells in physiological conditions (Figure 1) is reminiscent of Ca^{2+} activity observed *in vivo* in other tissues, including mouse skin epidermal stem cells and brain capillaries (4, 17). However, our uncovering of spatiotemporal conservation of Ca^{2+} activity and its large-scale coordination emerged as critical features of skin capillaries (Figure 1). Specifically, the discovery that EC network activity status is maintained on a cellular level and that the distribution of Ca^{2+} dynamics is conserved on a population level is a novel finding across organs and organisms to date. Large-scale coordination between ECs has been shown in periods of extensive vascular remodeling, such as development and injury (34, 36, 37, 51, 52). Our work establishes an unexpected paradigm that Ca^{2+} activity in capillaries is both orchestrated on a tissue-wide scale and is non-random in its spatial patterning. Heterogeneity between ECs in Ca^{2+} activity, which is conserved at a single-cell level over days to weeks, reveals molecular EC heterogeneity between cells in the same vascular compartment. This further builds upon EC heterogeneity that has been extensively described in the same vascular compartment, across the vascular tree, and between organs, to better allow ECs to adapt to their local environments (53-61). Our findings may indicate differences in microenvironment and/or decision-making on a cell-to-cell basis in skin capillaries.

Gap junction Cx43 exerts control over the active network on a temporal scale, regulating how network coordination maintains Ca^{2+} dynamics over time (Figure 2). Ca^{2+} activity in the Cx43ckO capillary plexus converges towards more persistent Ca^{2+} activity without any apparent cell death, while maintaining similar proportions of active ECs. Such perturbed network activity displays remarkable vascular resilience. Given the role of elevated, sustained cytosolic Ca^{2+} in

apoptosis and cell death, we anticipate that other molecular mechanisms might function to keep high concentrations of intracellular Ca^{2+} in check (62-64). Previous work has identified the protective effects of acetylcholine, PMCA (Plasma Membrane Ca^{2+}-ATPase), and SERCA (Sarco/Endoplasmic Reticulum Ca^{2+} ATPase) upregulation or overexpression in reducing Ca^{2+} overload and promoting cell survival (65-67). Thus, we wonder whether similar changes in our system might buffer Ca^{2+} concentration elevation below the threshold required for cell death. Our findings provide further insight into the spatial range of Cx43 as a mediator of Ca^{2+} communication between cells and indicate that it may serve to coordinate the extent and conservation of Ca^{2+} activity across a network over time.

The phenotype of persistently active cells in Cx43cKO mice (Figure 2) contrasts with *in vitro* and *ex vivo* work in ECs where pharmacological inhibition of pan-gap junctions, or genetic knockout of different Connexin isoforms such as Cx40 leads to decreases in Ca^{2+} activity (26, 29, 68-72). Specifically, in e*x vivo*, both Ca^{2+} activity and spreading between adjacent alveolar capillaries is abolished in EC-specific Cx43 knockout mice, or with a mimetic peptide that blocks Cx43 function (73). While *in vivo* Ca^{2+} activity is yet to be visualized in response to loss of gap junctions, the EC conditional deletion of Cx43, Cx37, and Cx40 leads to phenotypes typically observed downstream of increased Ca^{2+} activity, such as sustained vessel dilation, and increase of plasma nitric oxide (42, 74). Thus, what other features within a native environment with intact plexus architecture may be influencing cytoplasmic Ca^{2+} in ECs after loss of Cx43 remains underexplored.

The novel interplay we uncovered between aberrant L-type VGCC activity and Cx43 dysregulation (Figure 3) provides insight into how voltage gated channels can reshape the EC Ca^{2+} landscape when ECs lack the full complement of gap junction activity. While previous studies have shown conflicting results regarding L-type VGCC expression in capillaries (43, 44, 75-78), the relationship between Cx43 and L-type VGCC activity in capillary ECs requires further investigation. Changes in channel activation independent of expression are possible, since modifications to channel domains on L-type VGCCs are known to modulate the duration of Ca^{2+} influx (79-81). Past studies have also implicated Cx43 gap junctions in maintaining and altering cell membrane potential through their electrical coupling and ion exchange functions (82, 83), potentially allowing for membrane depolarization-mediated activation of L-type VGCCs and Ca^{2+} influx following the loss of Cx43.

Nifedipine may also affect Ca^{2+} activity in Cx43cKO ECs through channel independent or non-cell autonomous mechanisms. Nifedipine can affect VEGF release from ECs, nitric oxide availability, and increase neurotransmitter release in the EC microenvironment, which can all influence EC Ca^{2+} after Cx43cKO (84-87). Furthermore, pericytes are known to influence EC Ca^{2+} activity in other tissues and express L-type VGCCs (88, 89). Indeed, evidence from the brain microvasculature shows that TRPC3 and L-type VGCCs work in concert to affect pericyte function, proposing a model, where ligand-activated TRPC3 provides the membrane

depolarization needed for L-type VGCC opening (90). Thus, we acknowledge that future work is needed to fully understand the role of volage gated channels in the vascular capillary plexus.

In conclusion, our work provides insight with unprecedented spatial and temporal resolution into how spatiotemporally conserved networks of capillary ECs regulate tissue-wide Ca^{2+} activity, and provides new concepts to both the vascular biology and Ca^{2+} signaling fields.

Limitations of the study

In this study, we investigated characteristics and regulation of tissue-level Ca^{2+} activity across capillary ECs *in vivo*, focusing on the skin. One consideration is using a pan-endothelial driver (VECadherin promoter) that does not allow us to discern EC heterogeneity or perturb specific subpopulations of ECs. Drug treatment absorption into the skin can also be variable. This issue was addressed by assessing multiple regions of the plexus within the same mice before and after treatments. Nifedipine used at higher concentrations can also inhibit other membrane ion channels, including T-type VGCCs and Ca^{2+} activated K^+ channels ($KCa_{3.1}$), though with lower affinity than L-type VGCCs (48, 91, 92).

Materials and Methods

Mice

VECadCreER (93) mice were obtained from Ralf Adams (Max Planck, Muster, Germany), *Cx43*$^{fl/fl}$ (74, 94), *Rosa26-CAG-LSL-GCaMP6s* (95), *Rosa26-CAG-LSL-H2B-mCherry* (96), and *LSL-tdTomato* (95) mice were obtained from The Jackson Laboratory. All experimental mice were bred to a mixed CD1 albino background. Mice from experimental and control groups were randomly selected from either sex for live imaging experiments, and were within an adult age range of 2–4 months. The experiments were not randomized, and all experimentation involving animals were performed under the approval of the Yale School of Medicine Institutional Animal Care and Use Committee (IACUC).

In vivo imaging

Imaging procedures were adapted from those previously described (97). An isoflurane chamber was used to anesthetize mice, and then the mice were transferred to the imaging stage on a 37 °C heating pad. Mice were maintained on anesthesia throughout the course of recording with vaporized isoflurane delivered by a nose cone (1.25% in oxygen and air). The right paw was mounted on a custom-made stage and a glass coverslip was placed directly against the flat part of the paw. Image stacks were acquired with a A LaVision TriM Scope II (LaVision Biotec) laser scanning microscope with a Chameleon Vision II (Coherent) two-photon laser (using 940 nm for live imaging) and a Chameleon Discovery (Coherent) two-photon laser (using 1120 nm for live

imaging). A Nikon 25x/1 water immersion objective was used. Optical sections were scanned with a field of view of 0.3 x 0.3 mm^2. For all timelapse movies, the live mouse remained anesthetized for the length of the experiment and serial optical sections (3 µm steps for a total stack of 12 µm) were captured at intervals of 3.441s for a total of 200 (11 minutes 28 seconds for topical pharmacological experiments) or 300 frames (17 minutes 12 seconds total recording time). For revisits, the same region of live mouse skin was imaged across intervals of multiple days, and anatomical features of the paw, such as mouse digits, were used as landmarks for finding the same location.

Image analysis

Raw image stacks were imported into FIJI (ImageJ, National Institutes of Health) for analysis. Max or average (to select for persistently active behaviors specifically) Z stacks of sequential optical sections were chosen. Translational motion correction of timelapse movies was performed on Imaris software.

Analysis of Ca^{2+} for individual ECs: Segmentation of the H2B-mCherry signal was performed via the threshold and masking functions on FIJI. Through a custom MATLAB pipeline, the GCaMP6s fluorescence intensity of each masked region of interest (ROI as a proxy for a cell) every 100 frames was normalized to the minimum fluorescence intensity over that period (Figure S2). Any change in fluorescence over a threshold (50% increase above the minimum fluorescence intensity) was treated as a Ca^{2+} event, and the duration of each event, as well as the number of events per ROI was calculated (Figure S2). Frequency is described as the number of events per minute, with the lowest possible frequency of 0.0588 events/minute (1 event over the 17min 12s recording duration) or 0.001 Hz.

Analysis of Ca^{2+} for EC clusters: Segmentation of the GCaMP6s signal with manual masking was used to segment the vessel surface. Using our custom MATLAB pipeline, we divided the masked vessel surface into individual grids, 0.0076 x 0.0076 mm^2 and the fluorescence intensity of each grid ROI was normalized every 100 frames by taking the minimum fluorescence value over each period (Figure S2). Any change in GCaMP6s fluorescence over 50% of the minimum fluorescence intensity was identified as a Ca^{2+} event, and the duration of each event, as well as the number of events per ROI was calculated. To analyze EC clusters, adjacent grid ROIs that displayed Ca^{2+} events either at the same frame or one frame apart were considered part of the cluster. The maximum number of grids with connected activity was represented, and the H2B-mCherry segmented ROIs were added to each set of connected grids to determine the number of ECs involved in each cluster (Figure S2).

Quantitative PCR

RNA from isolated ECs was extracted using Qiagen RNeasy Plus Micro kit (74034). cDNA was made using SuperScript IV First-Strand Synthesis kit (Thermo Fisher 18091050). qPCR utilized FastStart Universal SYBR green Master (Sigma) on the CFX Connect Real-Time PCR Detection System (Bio-Rad). The set of primers used are as follows:

Connexin 37: forward, CCCACATCCGATACTGGGTG; reverse, CGAAGACGACCGTCCTCTG.

Connexin 40: forward, AGGGCTGAGCTTGCTTCTTA; reverse, TTAGTGCCAGTGTCGGGAAT.

Connexin 43: forward, GGTGATGAACAGTCTGCCTTTCG; reverse, GTGAGCCAAGTACAGGAGTGTG.

Tamoxifen induction

To induce the expression of GCaMP6s, H2B-mCherry, and/or loss of Cx43 expression, *VECadCreER; GCaMP6s; H2B-mCherry* or *VECadCreER; Cx43fl/fl; GCaMP6s; H2B-mCherry* or *VECadCreER; Cx43fl/fl; GCaMP6s* or *VECadCreER; GCaMP6s* or *VeCadCreER; Cx43fl/fl* or *VeCadCreER; tdtomato* or *VeCadCreER* mice were given four doses of tamoxifen (2 mg in corn oil) 4, 5, 6, and 7 days before imaging or tissue collection by intraperitoneal injection (IP).

Topical drug treatment

For each drug tested, 4-6 capillary regions were imaged for 200 frames (11 min 28 s). To inhibit Piezo1, TRPV4, or L-type Ca^{2+} channels, Dooku1, GSK219, and nifedipine respectively were delivered topically to the paw skin. Nifedipine and GSK219 were dissolved in a 100 mg ml^{-1} stock solution in dimethyl sulfoxide (DMSO) and 30 µl of the mixture was spread evenly on the paw for 15 minutes. Dooku1 was dissolved in a 60 mg ml^{-1} stock solution in dimethyl sulfoxide (DMSO) and 50 µl of the mixture was spread evenly on the paw for 15 minutes. Regions in the paw were then revisited 30-60 minutes after application of the topical agents. A solution of 100% DMSO was used as vehicle control.

Endothelial cell isolation and sorting

VECadCreER or *VECadCreER; tdtomato* mice were induced with tamoxifen 1 week prior to harvesting tissue. Adult paws were collected and placed dermis side down in a 5 mg/ml dispase II solution (MilliporeSigma; 494207800) for 45 minutes at 37 °C. The epidermis was removed, and the dermis was minced finely and transferred to 0.25% collagenase IV (Sigma; C5138) in HBSS (GIBCO;14170-112) solution for at least 90 minutes at 37 °C. The tissue was then passed through an 18-gauge needle (BD; 305195) and washed in FACS Buffer (3% FBS, 2mM EDTA). The suspensions were then centrifuged at 350G for 10 minutes and filtered through a 40 µm filter (Falcon; 352340) before staining with anti-mouse CD31 APC (Biolegend;160210; 1/200) for sorting on a BD FACS AriaII. ECs were sorted based on expression of CD31 (and for *tdtomato* in *VECadCreER; tdtomato mice*).

Statistics and reproducibility

GraphPad Prism software (GraphPad, Inc.) was used to perform statistical analyses (version 9.2). Parameters are reported in the figure legends, and comparisons between groups were made using paired or unpaired two-tailed Student's *t* test, or Chi-squared analysis for observed versus expected outcomes (df=1) in revisits. Normality was assumed in data distribution, but not formally tested. Differences between groups were considered significant at $P < 0.05$ and the data are presented as means ± SD.

High frequency or high average duration EC populations were designated as displaying activity 1 standard deviation (SD) greater than the mean of all active ECs. For wildtype revisits, the value threshold for >1SD dynamics cells was calculated based on frequency and average duration distributions on Day 0. For Cx43cKO mice, the value threshold for >1SD dynamics cells was based on the frequency and average duration distributions of the control mice.

For Chi-squared analysis, expected values of ECs active on Day 0 and then also when revisited ('random activity' as the null hypothesis) were assigned based on the percentage of ECs displaying activity on Day 0 (58% for 24-hour revisits, 54% for 14-day revisits, and 74% for Cx43cKO 14-day revisits). These proportions were then compared to the percentage of cells that were observed to maintain their activity status upon revisiting.

To assess changes in frequency and average duration dynamics in revisited regions after pharmacological application of DMSO or nifedipine, the mean values of frequency and average duration were calculated for each mouse before and after treatment, and the percentage change between the pre-treatment and post-treatment values was compared between the two conditions.

Acknowledgements

We thank all members of the Greco laboratory, especially S. Du and T. Xin, as well as B. Ehrlich, D. Greif, and Z. Sun (Yale), for critical feedback on the project as well as advice on tool development. This work was supported by National Institutes of Health grant nos. R01AR063663-12, R01AR072668-06, a Leo Foundation Grant LF-OC-23-001463, the Howard Hughes Medical Institute, and the European Research Council project no. 101167365 (all to VG), and a K99 award grant no. 5K99AR079555-02 (to CYK).

Author Contributions

AS, CYK, JJM, and VG conceived the project and designed experiments. AS, VG, JJM, CYK and DMA wrote the manuscript. AS performed and/or participated in all experiments and analyzed the data. DGG and JLM helped build the analysis pipeline. CMM performed flow

cytometry and qPCR experiments. DS and FX performed staining analyses. DGG, CMM, DS, FX, and JLM provided critical feedback to the manuscript text and schematics.

Figure 1

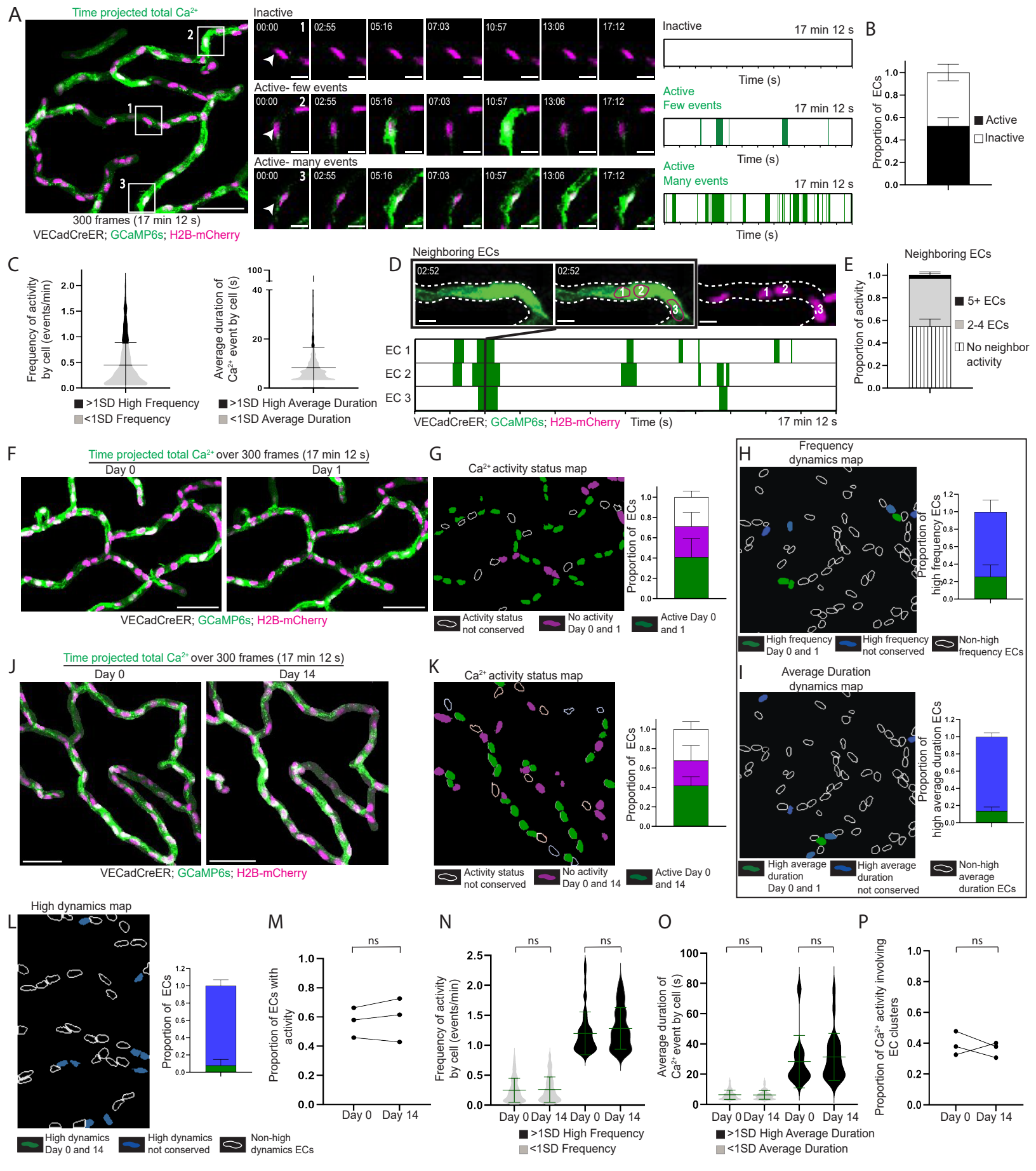
A
Time projected total Ca2+
300 frames (17 min 12 s)
VECadCreER; GCaMP6s; H2B-mCherry
Inactive
Active- few events
Active- many events
Inactive
Active Few events
Active Many events
17 min 12 s
Time (s)
B
Proportion of ECs
Active
Inactive
C
Frequency of activity by cell (events/min)
>1SD High Frequency
<1SD Frequency
Average duration of Ca2+ event by cell (s)
>1SD High Average Duration
<1SD Average Duration
D
Neighboring ECs
EC 1
EC 2
EC 3
VECadCreER; GCaMP6s; H2B-mCherry
Time (s)
17 min 12 s
E
Neighboring ECs
Proportion of activity
5+ ECs
2-4 ECs
No neighbor activity
F
Time projected total Ca2+ over 300 frames (17 min 12 s)
Day 0
Day 1
VECadCreER; GCaMP6s; H2B-mCherry
G
Ca2+ activity status map
Proportion of ECs
Activity status not conserved
No activity Day 0 and 1
Active Day 0 and 1
H
Frequency dynamics map
Proportion of high frequency ECs
High frequency Day 0 and 1
High frequency not conserved
Non-high frequency ECs
I
Average Duration dynamics map
Proportion of high average duration ECs
High average duration Day 0 and 1
High average duration not conserved
Non-high average duration ECs
J
Time projected total Ca2+ over 300 frames (17 min 12 s)
Day 0
Day 14
VECadCreER; GCaMP6s; H2B-mCherry
K
Ca2+ activity status map
Proportion of ECs
Activity status not conserved
No activity Day 0 and 14
Active Day 0 and 14
L
High dynamics map
Proportion of ECs
High dynamics Day 0 and 14
High dynamics not conserved
Non-high dynamics ECs
M
Proportion of ECs with activity
ns
Day 0
Day 14
N
Frequency of activity by cell (events/min)
ns
>1SD High Frequency
<1SD Frequency
O
Average duration of Ca2+ event by cell (s)
ns
>1SD High Average Duration
<1SD Average Duration
P
Proportion of Ca2+ activity involving EC clusters
ns

Figure 1

The skin capillary plexus displays Ca^{2+} activity orchestrated by a spatiotemporally conserved network of endothelial cells (A) *Left*: Max intensity projection of GCaMP6s signal (green) with H2B-mCherry signal (magenta) from 300 frame (17 min 12 s) recording of skin capillary ECs showing heterogenous Ca^{2+} activity between cells (scale bar: 50 µm). *Mid*: Insets of 3 different regions represent differences in Ca^{2+} activity between cells (scale bar: 10 µm). *Right*: Ca^{2+} events and their durations over the recording time for each of the ECs displayed in the insets (green represents Ca^{2+} activity) **(B)** Proportion of ECs displaying Ca^{2+} activity (active ECs in black and inactive ECs in white). *n*=14 regions from 4 mice. **(C)** Frequency of Ca^{2+} activity per cell (events/min) and average duration (s) of a Ca^{2+} event by cell across 1,765 ECs from 4 mice. EC groups represented by black (>1SD high activity) and grey (<1SD activity) **(D)** *Top*: Ca^{2+} activity occurring simultaneously across 3 ECs (numbered and drawn in magenta outline matching H2B-mCherry). *Bottom*: Ca^{2+} events and their durations over recording time for each EC (scale bar: 10 µm). Black line across plots indicates the timepoint when all 3 ECs simultaneously display Ca^{2+} activity. **(E)** Proportion of Ca^{2+} activity involving various EC cluster sizes. *n* = 14 regions from 4 mice. **(F)** Max intensity projection of GCaMP6s signal with H2B-mCherry signal, with the same regions revisited and recorded 24 hours later (scale bar: 50 µm). **(G)** *Left*: Ca^{2+} activity status map for ECs revisited after 24 hours in (F). Non-conserved activity status (white outline), inactive both days (magenta) and active both days (green). *Right*: Proportion of ECs by conservation of their activity status. Chi-square analysis (observed activity 24 hours after versus random activity as null hypothesis) P<0.0001. *n*=7 regions from 3 mice. **(H)** and **(I)** *Left*: Dynamics map for ECs revisited after 24 hours for conserved high frequency or high average duration behavior on Day 0 and Day 1 (green), not conserved (blue) or not observed (white outline) groups. *Right*: Conservation of >1SD dynamics behavior (green) as a proportion of total high frequency or high average duration ECs. *n*=7 regions from 3 mice. **(J)** Max intensity projection with the same region revisited and recorded 14 days later (scale bar: 50 µm). **(K)** *Left*: Ca^{2+} activity status map for ECs revisited after 14 days in (J). *Right*: Conservation of activity status as a proportion of total ECs. Chi-square (observed activity 14 days after versus random activity as null hypothesis) P<0.0001. *n*=8 regions from 3 mice. **(L)** *Left*: Dynamics map for ECs revisited after 14 days for conserved >1SD high dynamics (including both high frequency and high average duration). *Right*: Conservation of >1SD high dynamics behavior (green) as a proportion of total high frequency and high average duration ECs. *n*=8 regions from 3 mice. **(M)** Proportion of active ECs from 3 mice on Day 0 and Day 14; ns: P>0.05, paired two-tailed Student's t-test, *n*=457 total cells from 3 mice. **(N)** and **(O)** Frequency of Ca^{2+} activity per cell (events/min) and average duration (s) of Ca^{2+} events on Day 0 and Day 14. black (>1SD high activity) and grey (<1SD activity); ns: P>0.05, unpaired two-tailed Student's t-test, *n*=265 active cells from 3 mice. **(P)** Proportion of Ca^{2+} activity involving EC clusters from 3 mice on Day 0 and Day 14; ns: P>0.05, paired two-tailed Student's t-test.

Figure 2

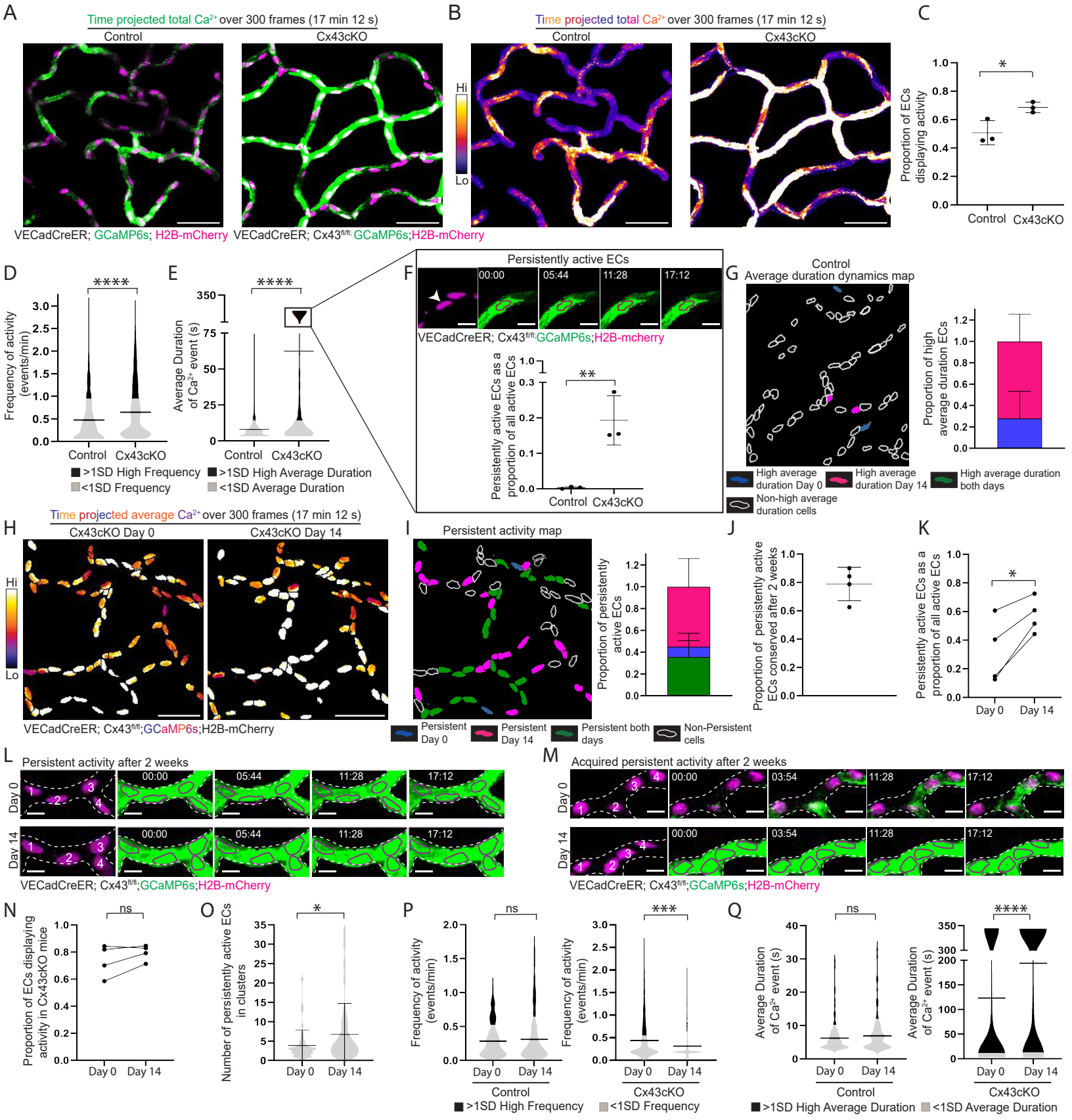
A
Time projected total Ca2+ over 300 frames (17 min 12 s)
Control
Cx43cKO
VECadCreER; GCaMP6s; H2B-mCherry
VECadCreER; Cx43fl/fl; GCaMP6s;H2B-mCherry
B
Time projected total Ca2+ over 300 frames (17 min 12 s)
Control
Cx43cKO
Hi
Lo
C
Proportion of ECs displaying activity
Control
Cx43cKO
D
Frequency of activity (events/min)
Control
Cx43cKO
>1SD High Frequency
<1SD Frequency
E
Average Duration of Ca2+ event (s)
Control
Cx43cKO
>1SD High Average Duration
<1SD Average Duration
F
Persistently active ECs
00:00
05:44
11:28
17:12
VECadCreER; Cx43fl/fl;GCaMP6s;H2B-mcherry
Persistently active ECs as a proportion of all active ECs
Control
Cx43cKO
G
Control
Average duration dynamics map
Proportion of high average duration ECs
High average duration Day 0
High average duration Day 14
High average duration both days
Non-high average duration cells
H
Time projected average Ca2+ over 300 frames (17 min 12 s)
Cx43cKO Day 0
Cx43cKO Day 14
Hi
Lo
VECadCreER; Cx43fl/fl;GCaMP6s;H2B-mCherry
I
Persistent activity map
Proportion of persistently active ECs
Persistent Day 0
Persistent Day 14
Persistent both days
Non-Persistent cells
J
Proportion of persistently active ECs conserved after 2 weeks
K
Persistently active ECs as a proportion of all active ECs
Day 0
Day 14
L
Persistent activity after 2 weeks
Day 0
Day 14
00:00
05:44
11:28
17:12
VECadCreER; Cx43fl/fl;GCaMP6s;H2B-mCherry
M
Acquired persistent activity after 2 weeks
Day 0
Day 14
00:00
03:54
11:28
17:12
VECadCreER; Cx43fl/fl;GCaMP6s;H2B-mCherry
N
Proportion of ECs displaying activity in Cx43cKO mice
Day 0
Day 14
O
Number of persistently active ECs in clusters
Day 0
Day 14
P
Frequency of activity (events/min)
Control
Cx43cKO
>1SD High Frequency
<1SD Frequency
Q
Average Duration of Ca2+ event (s)
Control
Cx43cKO
>1SD High Average Duration
<1SD Average Duration

Figure 2

Loss of endothelial Connexin 43 leads to sustained Ca^{2+} dynamics and impairs long-term network regulation (A) Max intensity projection of GCaMP6s signal (green) with H2B-mCherry signal (magenta) from 300 frame (17 min 12 s) recording of skin capillary ECs from control (VECadCreER; GCaMP6s; H2B-mCherry) and Cx43cKO (VECadCreER; $Cx43^{fl/fl}$; GCaMP6s; H2B-mCherry) mice (scale bar: 50 µm). **(B)** Max intensity projection of GCaMP6s signal from (A) represented with fire lookup table. Color scale indicates GCaMP6s signal over total duration of recording (scale bar: 50 µm). **(C)** Proportion of active ECs in control and Cx43cKO mice. P=0.0288, unpaired two-tailed Student's t-test; *n*=10 regions from 3 mice each for control and Cx43cKO. **(D) and (E)** Frequency of Ca^{2+} activity per cell (events/min) and average duration (s) of a Ca^{2+} event by cell respectively for control and Cx43cKO; black (>1SD high activity) and grey (<1SD activity)**.** *n*=570 active ECs from 3 control mice and 837 active ECs from 3 Cx43cKO mice; P<0.0001 for both, unpaired two-tailed Student's t-test. **(F)** *Top*: Representative EC (drawn in magenta outline corresponding with H2B-mCherry label) displaying persistent activity in Cx43cKO mouse (scale bar: 10 µm). *Bottom*: Persistently active ECs as a proportion of total active ECs in control and Cx43cKO mice; P=0.009, unpaired two-tailed Student's t-test. **(G)** *Left:* Representative average duration cells map of control ECs revisited after 14 days. High average duration ECs on Day 0 (blue), Day 14 (magenta) or both days (green), and non-high average duration ECs (white outline) *Right:* Bar graph of high average duration ECs on day 0, 14, or both days. *n*=4 regions from 3 mice **(H)** Average intensity projections of GCaMP6s signal over H2B-mCherry region for single-cell resolution (fire lookup table) in Cx43cKO ECs revisited after 14 days (scale bar: 50 µm). Color scale indicates average GCaMP6s signal over total duration of recording. Average intensity projection provides visualization of persistently active ECs in white. **(I)** *Left*: Persistent activity map of ECs revisited after 14 days. Persistently active ECs on Day 0 (blue), Day 14 (magenta) or both days (green), and non-persistently active ECs (white outline). *Right*: Bar graph of persistently active ECs on Day 0, 14, or both days. *n=7* regions from 4 mice. **(J)** Proportion of persistently active ECs conserved after 14 days among revisited mice. **(K)** Persistently active ECs as a proportion of all active ECs, in mice revisited after 14 days; P=0.023, paired two-tailed Student's t-test. *n=7* regions from 4 mice. **(L)** Representative image of ECs (numbered and drawn in magenta outline of H2B-mCherry signal) maintaining persistent activity after 14 days in Cx43cKO mouse (scale bar: 10 µm). **(M)** Representative image of ECs gaining persistent activity on Day 14 (scale bar: 10 µm). **(N)** Proportion of active ECs from 4 Cx43cKO mice on Day 0 and Day 14; ns: P>0.05, paired two-tailed Student's t-test, *n*=532 total cells from 4 mice. **(O)** Number of persistently active ECs in clusters, for regions revisited after 14 days; P=0.047, unpaired two-tailed Student's t-test. **(P)** Frequency of Ca^{2+} activity per cell (events/min) and average duration **(Q)** of Ca^{2+} events by cell (s) on Day 0 and Day 14 of revisited ECs in control and Cx43cKO mice; black (>1SD high activity) and grey (<1SD activity). P<0.0001, unpaired two-tailed Student's t-test in Cx43cKO mice; *n*=399 active cells from 4 mice**.** ns= P>0.05, unpaired two-tailed Student's t-test in control mice, *n*=126 active cells from 3 mice.

Figure 3

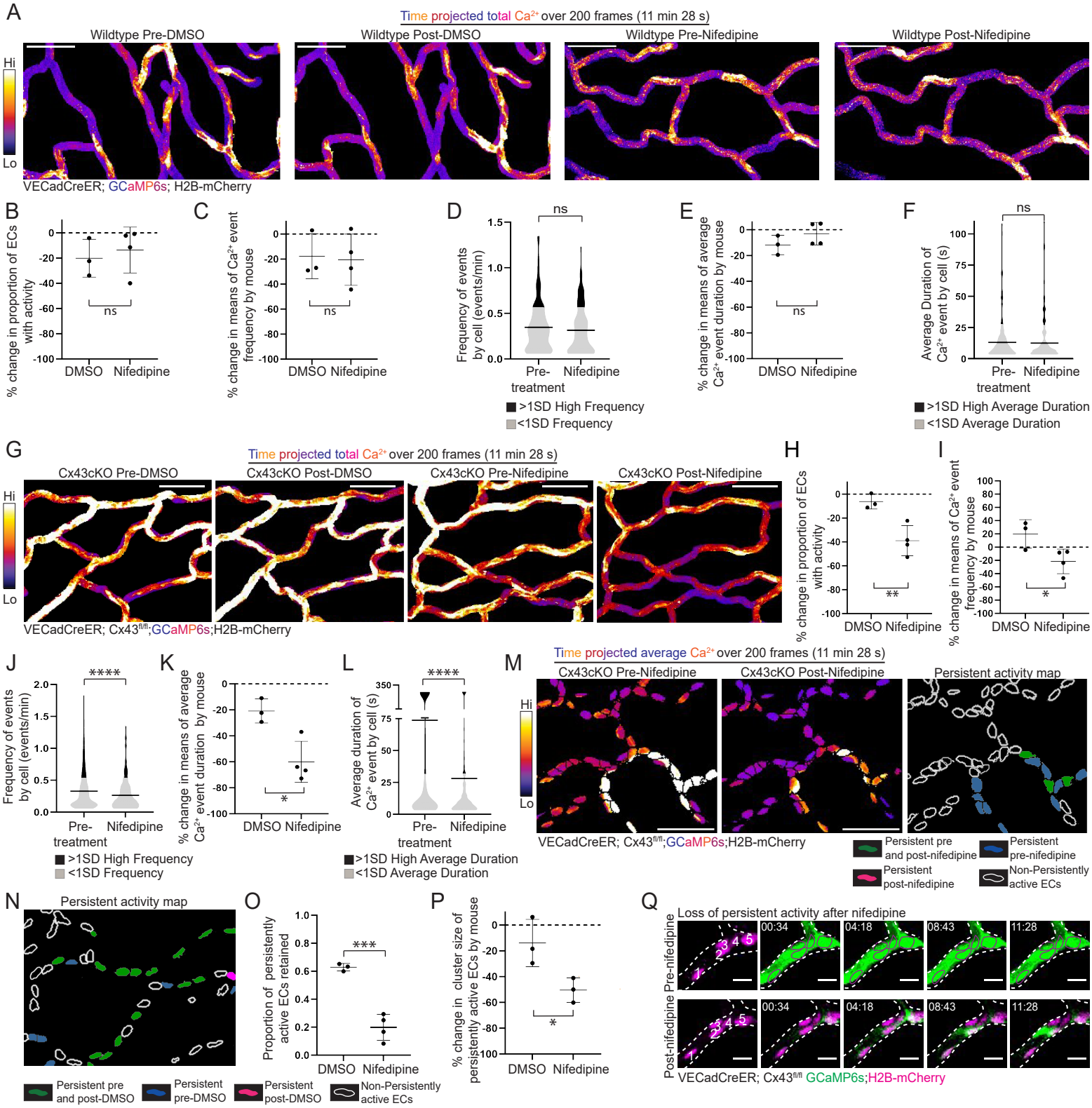
A
Time projected total Ca2+ over 200 frames (11 min 28 s)
Wildtype Pre-DMSO
Wildtype Post-DMSO
Wildtype Pre-Nifedipine
Wildtype Post-Nifedipine
Hi
Lo
VECadCreER; GCaMP6s; H2B-mCherry
B
% change in proportion of ECs with activity
ns
DMSO Nifedipine
C
% change in means of Ca2+ event frequency by mouse
ns
DMSO Nifedipine
D
Frequency of events by cell (events/min)
ns
Pre-treatment
Nifedipine
>1SD High Frequency
<1SD Frequency
E
% change in means of average Ca2+ event duration by mouse
ns
DMSO Nifedipine
F
Average Duration of Ca2+ event by cell (s)
ns
Pre-treatment
Nifedipine
>1SD High Average Duration
<1SD Average Duration
G
Time projected total Ca2+ over 200 frames (11 min 28 s)
Cx43cKO Pre-DMSO
Cx43cKO Post-DMSO
Cx43cKO Pre-Nifedipine
Cx43cKO Post-Nifedipine
Hi
Lo
VECadCreER; Cx43fl/fl;GCaMP6s;H2B-mCherry
H
% change in proportion of ECs with activity
**
DMSO Nifedipine
I
% change in means of Ca2+ event frequency by mouse
*
DMSO Nifedipine
J
Frequency of events by cell (events/min)
****
Pre-treatment
Nifedipine
>1SD High Frequency
<1SD Frequency
K
% change in means of average Ca2+ event duration by mouse
*
DMSO Nifedipine
L
Average duration of Ca2+ event by cell (s)
****
Pre-treatment
Nifedipine
>1SD High Average Duration
<1SD Average Duration
M
Time projected average Ca2+ over 200 frames (11 min 28 s)
Cx43cKO Pre-Nifedipine
Cx43cKO Post-Nifedipine
Persistent activity map
Hi
Lo
VECadCreER; Cx43fl/fl;GCaMP6s;H2B-mCherry
Persistent pre and post-nifedipine
Persistent pre-nifedipine
Persistent post-nifedipine
Non-Persistently active ECs
N
Persistent activity map
Persistent pre and post-DMSO
Persistent pre-DMSO
Persistent post-DMSO
Non-Persistently active ECs
O
Proportion of persistently active ECs retained
***
DMSO Nifedipine
P
% change in cluster size of persistently active ECs by mouse
*
DMSO Nifedipine
Q
Loss of persistent activity after nifedipine
Pre-nifedipine
Post-nifedipine
00:34
04:18
08:43
11:28
VECadCreER; Cx43fl/fl GCaMP6s;H2B-mCherry

Figure 3

L-type Ca^{2+} channels regulate sustained Ca^{2+} dynamics after Cx43cKO, but do not affect Ca^{2+} activity under physiological conditions (A) Max intensity projection of GCaMP6s signal in wildtype mice before and after treatment with either DMSO or nifedipine. GCaMP6s signal is represented with fire lookup table from 200 frame (11 min 28 s) recording of skin capillary ECs before and after treatment. Color scale indicates GCaMP6s signal over recording time (scale bar: 50 µm). **(B)** Percent change in proportion of active ECs in wildtype mice revisited after treatment with either DMSO or nifedipine. ns=P>0.05, unpaired two-tailed Student's t-test; *n*= 5 regions from 3 mice for DMSO treatment and 6 regions from 4 mice for nifedipine treatment. **(C)** and **(E)** Percent change in frequency (events/min) and average duration (s) dynamics of ECs in wildtype mice revisited after treatment with either DMSO or nifedipine (shown as percentage change of means, refer to Methods under Statistics and Reproducibility). ns=P>0.05, unpaired two-tailed Student's t-test. **(D)** and **(F)** Frequency of Ca^{2+} activity per cell (events/min) and average duration of Ca^{2+} events by cell (s) of revisited wildtype mice before and after nifedipine treatment. black (>1SD high activity) and grey (<1SD activity); ns=P>0.05, unpaired two-tailed Student's t-test; *n*=187 active ECs pre-treatment and *n*=173 active ECs after treatment, from 4 mice**. (G)** Max intensity projection of GCaMP6s signal in Cx43cKO mice before and after treatment with either DMSO or nifedipine. (scale bar: 50 µm). **(H)** Percent change in proportion of active ECs in Cx43cKO mice revisited after treatment with either DMSO or nifedipine. P=0.0097, unpaired two-tailed Student's t-test; *n*=5 regions from 3 mice for DMSO treatment and 6 regions from 4 mice for nifedipine treatment. **(I)** and **(K)** Percent change in frequency (events/min) and average duration (s) dynamics of ECs in Cx43cKO mice revisited after treatment with either DMSO or nifedipine. P=0.04, unpaired two-tailed Student's t-test, for frequency plot. P=0.013, unpaired two-tailed Student's t-test, for average duration plot. **(J)** and **(L)** Violin plots showing frequency of Ca^{2+} activity per cell (events/min) and average duration (s) of Ca^{2+} events by cell of revisited regions before and after nifedipine treatment. black (>1SD high activity) and grey (<1SD activity); P<0.0001, unpaired two-tailed Student's t-test; *n*=358 active ECs pre-treatment and *n*=218 active ECs after treatment, from 4 mice**. (M)** *Left:* Average intensity projections of GCaMP6s signal (fire lookup table) over H2B-mCherry region for single-cell resolution, from regions revisited after nifedipine treatment (scale bar: 50 µm). Color scale indicates average GCaMP6s signal over total recording time. Average intensity projection improves visualization of persistently active ECs in white. *Right*: Map of persistently active ECs after nifedipine treatment. Persistently active ECs pre- and post-nifedipine (green), pre-nifedipine (blue), post-nifedipine (magenta) or non-persistently active ECs (white outline). **(N) and (O)** *Left*: Representative map of persistently active ECs in Cx43cKO mice revisited after treatment with DMSO. *Right*: Proportion of persistently active ECs retained after DMSO versus nifedipine treatments. *n*=5 regions from 3 mice for DMSO and 6 regions from 4 mice for nifedipine treatment. **(P)** Percent change in cluster size of persistently active ECs revisited after treatment with either DMSO or nifedipine; P=0.038, unpaired two-tailed Student's t-test. **(Q)** Representative images of ECs without persistent activity after nifedipine treatment in a Cx43cKO mouse (scale bar: 10 µm).

Figure 4

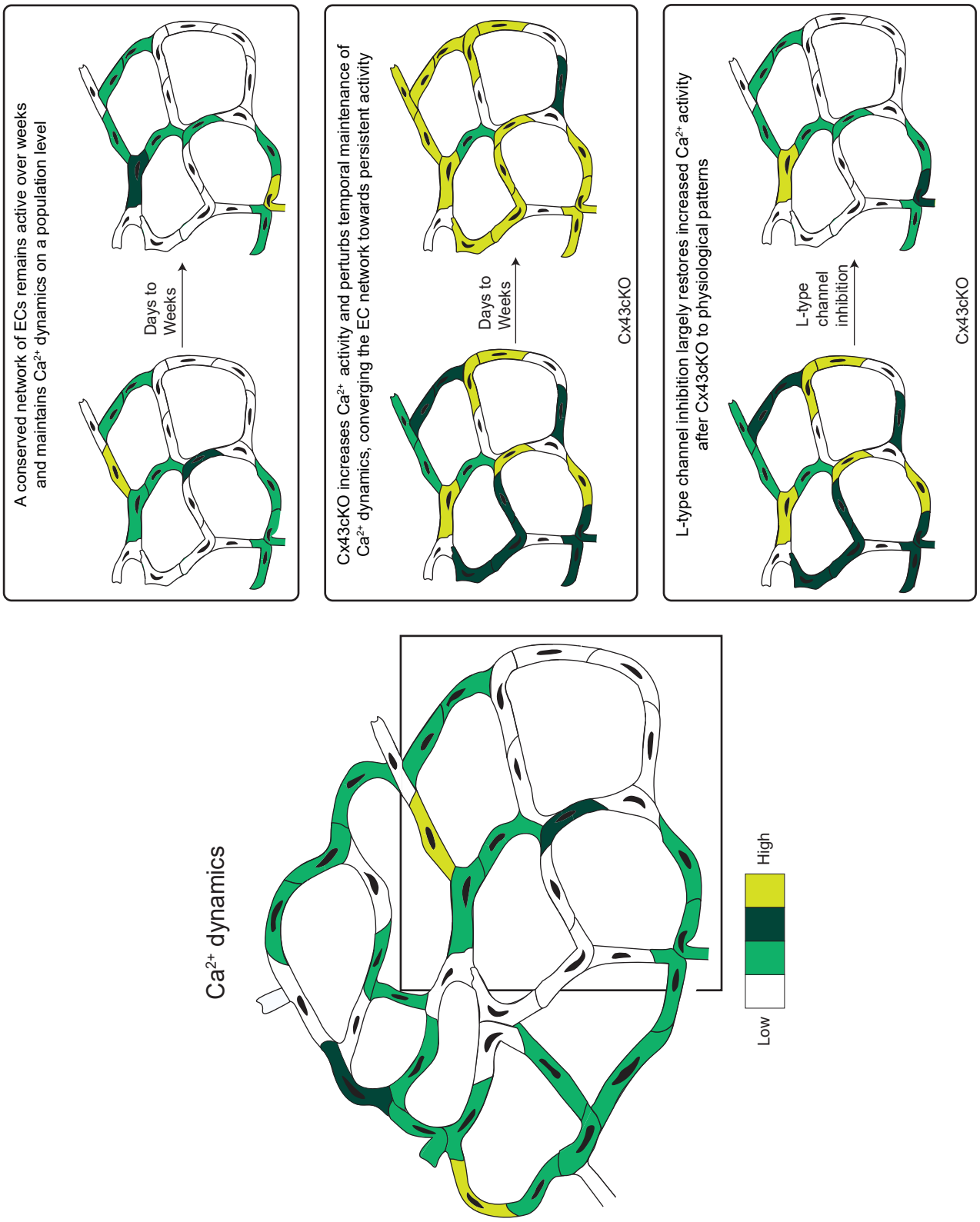
A conserved network of ECs remains active over weeks and maintains Ca^{2+} dynamics on a population level
Days to Weeks
Cx43cKO increases Ca^{2+} activity and perturbs temporal maintenance of Ca^{2+} dynamics, converging the EC network towards persistent activity
Days to Weeks
Cx43cKO
L-type channel inhibition largely restores increased Ca^{2+} activity after Cx43cKO to physiological patterns
L-type channel inhibition
Cx43cKO
Ca^{2+} dynamics
Low
High

Figure 4

A conserved network orchestrates spatiotemporal Ca^{2+} patterning in capillary ECs over days to weeks and is regulated by Cx43. Model depicting the spatiotemporal characteristics of Ca^{2+} signaling organization in capillary ECs. A spatiotemporally conserved network of ECs orchestrates tissue-wide Ca^{2+} activity over days to weeks and maintains Ca^{2+} dynamics at the population level. Loss of Cx43 increases Ca^{2+} activity and impairs long-term temporal regulation of the EC network, converging on a persistently active phenotype. L-type VGCC inhibition largely restores Ca^{2+} activity in Cx43cKO mice to physiological activity patterns.

Figure S1

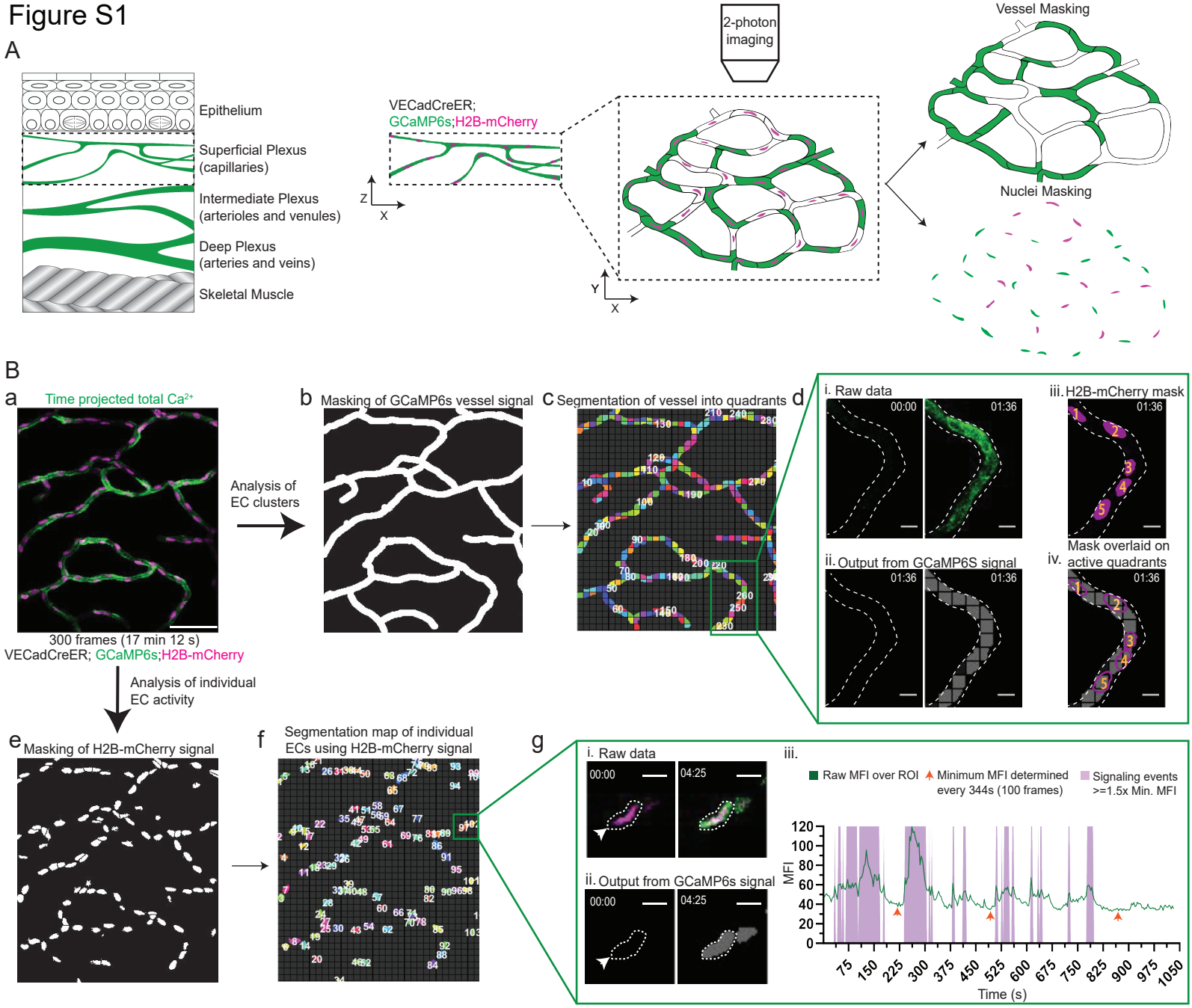
A
Epithelium
Superficial Plexus (capillaries)
Intermediate Plexus (arterioles and venules)
Deep Plexus (arteries and veins)
Skeletal Muscle
VECadCreER; GCaMP6s;H2B-mCherry
Z
X
2-photon imaging
Y
X
Vessel Masking
Nuclei Masking
B
a
Time projected total Ca2+
300 frames (17 min 12 s)
VECadCreER; GCaMP6s;H2B-mCherry
Analysis of EC clusters
b
Masking of GCaMP6s vessel signal
c
Segmentation of vessel into quadrants
d
i. Raw data
00:00
01:36
ii. Output from GCaMP6S signal
iii. H2B-mCherry mask
iv. Mask overlaid on active quadrants
Analysis of individual EC activity
e
Masking of H2B-mCherry signal
f
Segmentation map of individual ECs using H2B-mCherry signal
g
i. Raw data
00:00
04:25
ii. Output from GCaMP6s signal
iii.
Raw MFI over ROI
Minimum MFI determined every 344s (100 frames)
Signaling events >=1.5x Min. MFI
MFI
Time (s)

Figure S1

Schematic of intravital imaging and analysis platforms in Ca^{2+} sensor mice (A) *Left*: Cartoon representing skin in XZ plane, outlining the superficial capillary plexus. *Middle*: Cartoon of 2-photon imaging over the XY plane of the capillary region, with EC-specific GCaMP6s signal (green) and H2B-mCherry signal (magenta). *Right*: Representation of vessel and nuclei masking from imaged regions. **(B) (a)** Max intensity projection of GCaMP6s signal (green) with H2B-mCherry signal (magenta) from 300 frame (17 min 12 s) recording of skin capillary ECs (scale bar: 50 µm). **(b) and (c)** Masking of vessels based on GCaMP6s signal, and segmentation of vessel mask into 0.0076 x 0.0076 mm^2 quadrants. **(d) (i)** Representative images of a Ca^{2+} event, with the **(ii)** pipeline output displaying the number of quadrants involved (scale bar: 10 µm). An event is defined as at least a 50% increase above mean fluorescence intensity (MFI) over the minimum fluorescence for each quadrant. **(iii) and (iv)** Adding the H2B-mCherry signal over the pipeline output allows determining the number of ECs involved. **(e)** Masking of nuclei based on H2B-mCherry signal as a proxy for individual ECs **(f)** Segmentation of nuclei mask into individual regions of interest (ROIs) **(g) (i)** Representative images of a Ca^{2+} event (scale bar: 10 µm), with the **(ii)** pipeline output displaying an event. An event is defined as at least a 50% increase above MFI over the minimum fluorescence for each ROI. **(iii)** MFI (green) over the ROI over 300 frames of recording (17 min 12 s), with minimum MFI calculated every 100 frames (orange arrowheads), and overlaid output Ca^{2+} events (purple).

Figure S2

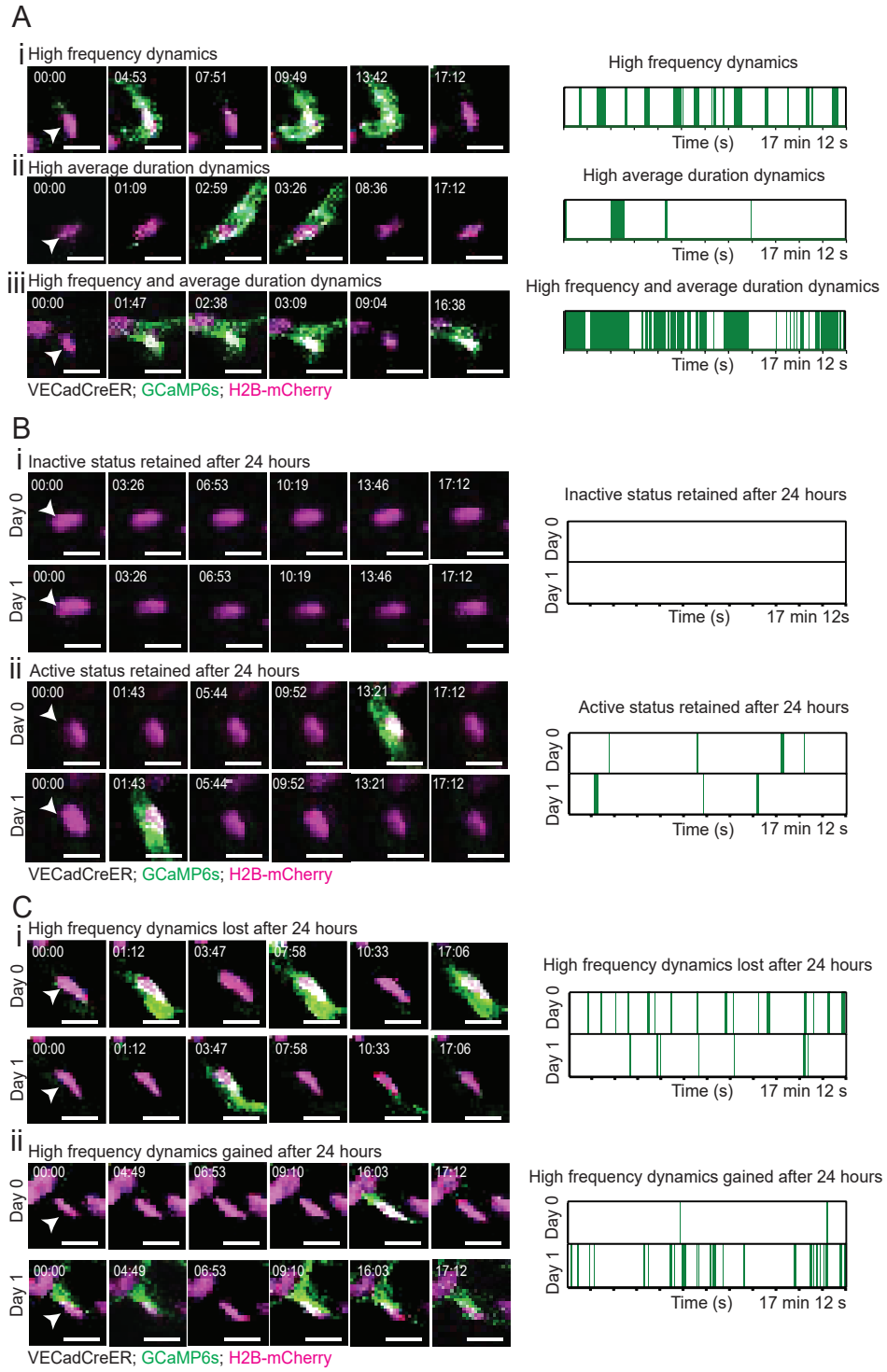
A
i High frequency dynamics
00:00
04:53
07:51
09:49
13:42
17:12
ii High average duration dynamics
00:00
01:09
02:59
03:26
08:36
17:12
iii High frequency and average duration dynamics
00:00
01:47
02:38
03:09
09:04
16:38
VECadCreER; GCaMP6s; H2B-mCherry
High frequency dynamics
Time (s)
17 min 12 s
High average duration dynamics
Time (s)
17 min 12 s
High frequency and average duration dynamics
Time (s)
17 min 12 s
B
i Inactive status retained after 24 hours
Day 0
Day 1
00:00
03:26
06:53
10:19
13:46
17:12
ii Active status retained after 24 hours
Day 0
Day 1
00:00
01:43
05:44
09:52
13:21
17:12
VECadCreER; GCaMP6s; H2B-mCherry
Inactive status retained after 24 hours
Day 0
Day 1
Time (s)
17 min 12s
Active status retained after 24 hours
Day 0
Day 1
Time (s)
17 min 12 s
C
i High frequency dynamics lost after 24 hours
Day 0
Day 1
00:00
01:12
03:47
07:58
10:33
17:06
ii High frequency dynamics gained after 24 hours
Day 0
Day 1
00:00
04:49
06:53
09:10
16:03
17:12
VECadCreER; GCaMP6s; H2B-mCherry
High frequency dynamics lost after 24 hours
Day 0
Day 1
Time (s)
17 min 12 s
High frequency dynamics gained after 24 hours
Day 0
Day 1
Time (s)
17 min 12 s

Figure S2

ECs retain activity status but can change dynamics after 24 hours (A) *Top*: Representative image of EC (nuclei in magenta) displaying high frequency dynamics with plot showcasing Ca^{2+} events (green) and their durations over 300 frames (17 min 12 s) of recording (scale bar: 10 µm). *Middle*: EC displaying high average duration dynamics. *Bottom*: EC displaying high frequency and high average duration dynamics. **(B) (i)** Representative image of EC displaying inactive status on Day 0 and again when revisited 24 hours later, (scale bar: 10 µm). **(ii)** EC displaying activity on Day 0 and again when revisited 24 hours later. **(C) (i)** Representative image of EC losing high frequency dynamics when revisited 24 hours later. (scale bar: 10 µm). **(ii)** EC gaining high frequency dynamics when revisited 24 hours later.

Figure S3

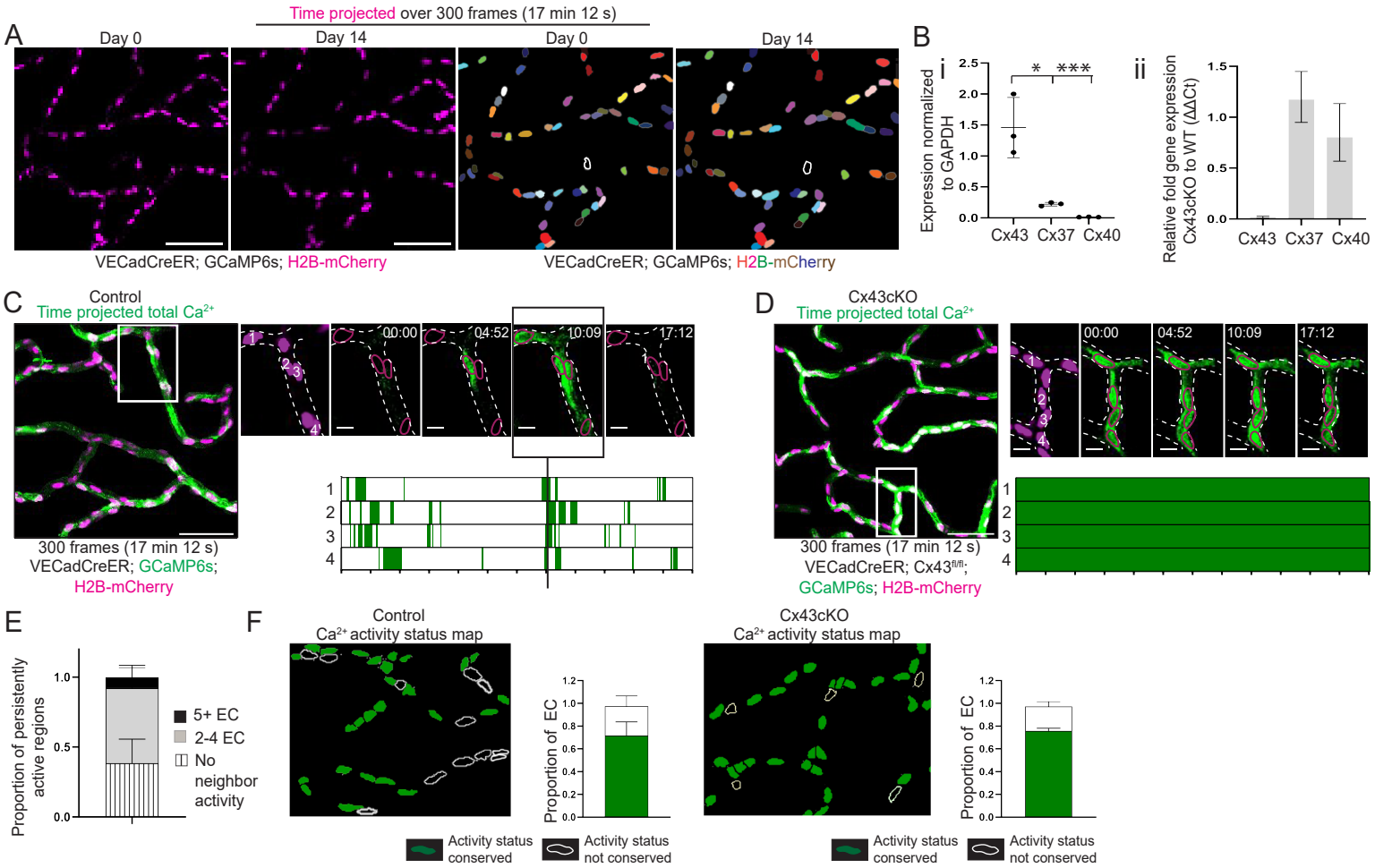
A
Time projected over 300 frames (17 min 12 s)
Day 0
Day 14
Day 0
Day 14
VECadCreER; GCaMP6s; H2B-mCherry
VECadCreER; GCaMP6s; H2B-mCherry
B
i
Expression normalized to GAPDH
Cx43
Cx37
Cx40
ii
Relative fold gene expression Cx43cKO to WT (ΔΔCt)
C
Control
Time projected total Ca2+
00:00
04:52
10:09
17:12
300 frames (17 min 12 s)
VECadCreER; GCaMP6s; H2B-mCherry
D
Cx43cKO
Time projected total Ca2+
300 frames (17 min 12 s)
VECadCreER; Cx43fl/fl; GCaMP6s; H2B-mCherry
E
Proportion of persistently active regions
5+ EC
2-4 EC
No neighbor activity
F
Control
Ca2+ activity status map
Proportion of EC
Cx43cKO
Ca2+ activity status map
Proportion of EC
Activity status conserved
Activity status not conserved
Activity status conserved
Activity status not conserved

Figure S3

Spatial and molecular analyses of Ca^{2+} dynamics across wildtype and Cx43cKO mice (**A)** *Left:* Representative image of region revisited on Day 0 and Day 14. *Right:* ECs multi-color coded, with the same colors on Day 0 and Day 14 corresponding to the same EC. **(B) (i)** Expression of vascular Connexins (Cx43, Cx37, and Cx40) in sorted skin ECs, normalized to GAPDH expression. *n*= 3 mice. **(ii)** Relative expression ($\Delta\Delta C_t$ method) of vascular Connexins after Cx43cKO, compared to control mice. Connexin expression in Cx43cKO mice is first normalized to GAPDH, and then to expression in wildtype mice. *n*= 3 Cx43cKO and *n*=3 control mice. (**C)** *Left*: Max intensity projection of GCaMP6s signal (green) with H2B-mCherry signal (magenta) from 300 frame (17 min 12 s) recording of skin capillary ECs in control mice (scale bar: 50 µm). *Right*: Inset of a region with Ca^{2+} activity occurring simultaneously across 4 ECs (numbered and drawn in magenta outline matching H2B-mCherry) (scale bar: 10 µm). *Bottom*: Ca^{2+} events and their durations over recording time for each EC (scale bar: 10 µm). Outline of the EC H2B-mCherry signal is shown in magenta. Black line across plots indicates the timepoint when all 4 ECs simultaneously display Ca^{2+} activity. **(D)** *Left*: GCaMP6s and H2B-mCherry signal from skin capillary ECs in Cx43cKO mice (scale bar: 50 µm). *Right*: Inset of a region with Ca^{2+} activity occurring simultaneously across 4 persistently active ECs (scale bar: 10 µm). *Bottom*: Ca^{2+} events for each persistently active EC. **(E)** Proportion of persistently active ECs involving different cluster sizes. *n* = 10 regions from 3 mice. **(F)** *Left*: Ca^{2+} activity status map for control ECs revisited after 14 days. Non-conserved activity status (white outline) and conserved activity status (green). Proportion of ECs by their conservation of activity status. Chi-square analysis (observed 14 days after versus random activity as null hypothesis) $P<0.0001$. *n*= 4 regions from 3 mice. *Right*: Ca^{2+} activity status map for Cx43cKO ECs revisited after 14 days. Proportion of ECs by their conservation of activity status. Chi-square analysis $P<0.0001$. *n*= 7 regions from 4 mice.

Figure S4

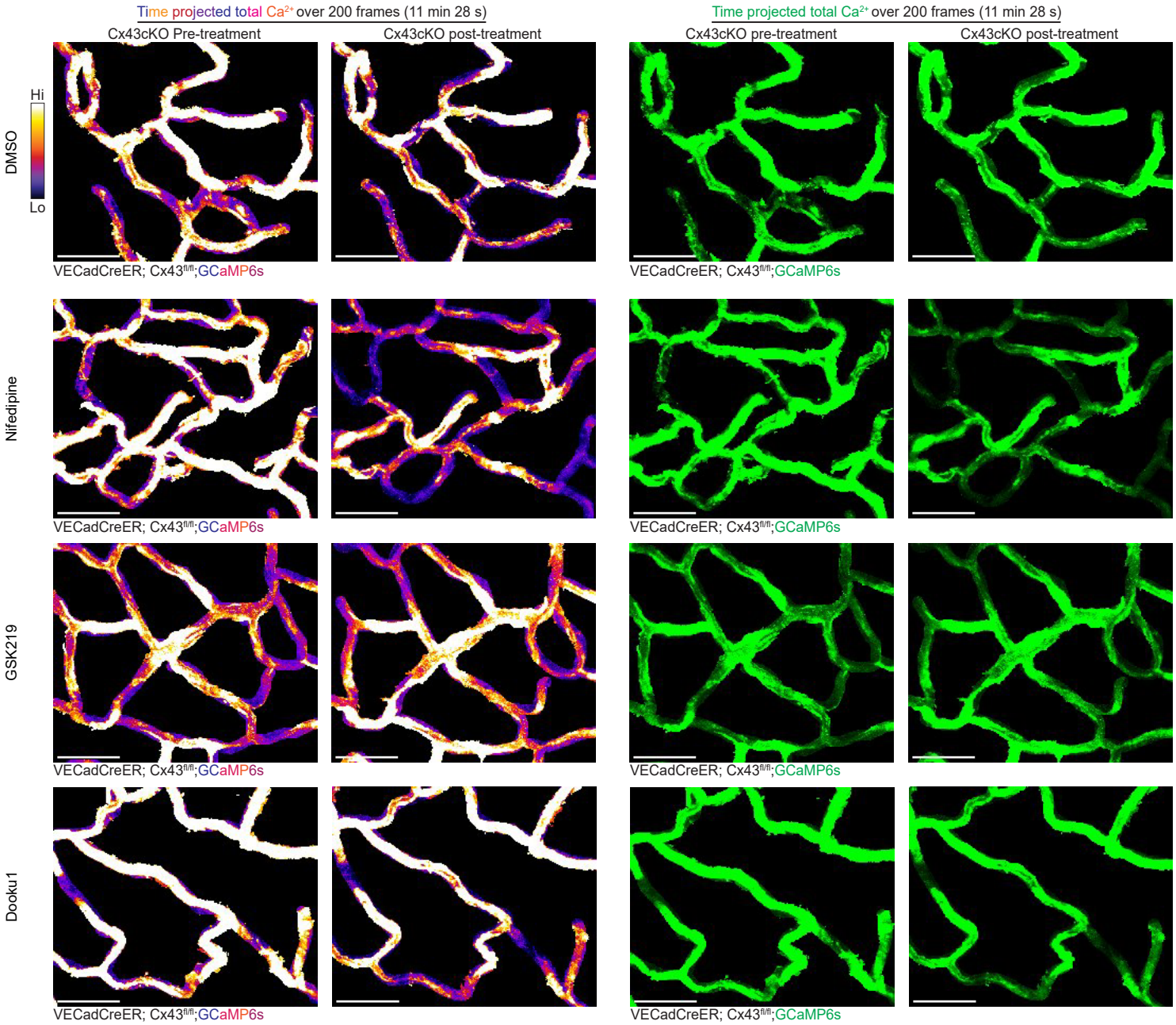
Time projected total Ca2+ over 200 frames (11 min 28 s)
Cx43cKO Pre-treatment
Cx43cKO post-treatment
Time projected total Ca2+ over 200 frames (11 min 28 s)
Cx43cKO pre-treatment
Cx43cKO post-treatment
Hi
Lo
DMSO
Nifedipine
GSK219
Dooku1
VECadCreER; Cx43fl/fl;GCaMP6s

Figure S4

L-type VGCC inhibition, relative to inhibiting Piezo1 and TRPV4, decreases Ca^{2+} activity after loss of Cx43 Max intensity projection of GCaMP6s signal in green and fire lookup table from 200 frame (11 min 28s) recording of skin capillary ECs in Cx43cKO mice before and after treatment with DMSO, nifedipine, GSK219, and Dooku1 (scale bar: 50 µm).

Movie 1 EC Ca^{2+} activity in skin capillaries is widespread and heterogenous during homeostasis Timelapse of GCaMP6s signal (green) and H2B-mCherry (magenta) from 300 frame (17 min 12 s) recording of skin capillary ECs, imaged at a frame rate of 3.441s/frame (scale bar: 20 µm). Timelapse is followed by a max intensity projection of GCaMP6s signal represented with fire lookup table. Color scale indicates GCaMP6s signal over recording time.

Movie 2 EC Ca^{2+} activity status is conserved on a single-cell level after 24 hours *Left*: Timelapse of GCaMP6s signal (green) and H2B-mCherry (magenta) from 300 frame (17 min 12 s) recording of skin capillary ECs on baseline Day 0, imaged at a frame rate of 3.441s/frame (scale bar: 20 µm). *Right:* Timelapse of region from Day 0 revisited after 24 hours. Timelapse is followed by a max intensity projection of GCaMP6s signal for Day 0 and Day 1 represented with fire lookup table. Color scale indicates GCaMP6s signal over recording time.

Movie 3 EC Ca^{2+} activity status is conserved on a single-cell level after 14 days *Left*: Timelapse of GCaMP6s signal (green) and H2B-mCherry (magenta) from 300 frame (17 min 12 s) recording of skin capillary ECs on baseline Day 0, imaged at a frame rate of 3.441s/frame (scale bar: 20 µm). *Right:* Timelapse of region from Day 0 revisited after 2 weeks. Timelapse is followed by a max intensity projection of GCaMP6s signal for Day 0 and Day 14 represented with fire lookup table. Color scale indicates GCaMP6s signal over recording time.

Movie 4 Cx43cKO leads to sustained EC Ca^{2+} activity *Left*: Timelapse of GCaMP6s signal (green) and H2B-mCherry (magenta) from 300 frame (17 min 12 s) recording of skin capillary ECs from control (WT) mice, imaged at a frame rate of 3.441s/frame (scale bar: 20 µm). *Right:* Timelapse of capillary ECs from Cx43cKO mice. Timelapse is followed by a max intensity projection of GCaMP6s signal for control and Cx43cKO mice, represented with fire lookup table. Color scale indicates GCaMP6s signal over recording time.

Movie 5 Cx43cKO leads to increase in persistently active ECs after 2 weeks *Left*: Timelapse of GCaMP6s signal (green) and H2B-mCherry (magenta) from 300 frame (17 min 12 s) recording of skin capillary ECs from Cx43cKO mice on baseline Day 0, imaged at a frame rate of 3.441s/frame (scale bar: 20 µm). *Right:* Timelapse of region from Day 0 revisited after 2 weeks, on Day 14. Timelapse is followed by an average intensity projection of GCaMP6s signal for Cx43cKO mice on Day 0 and Day 14, represented with fire lookup table. Average intensity projections allow better visualization of persistently active regions. Color scale indicates GCaMP6s signal over recording time.

Movie 6 L-type VGCC inhibition does not affect EC Ca^{2+} activity in wildtype mice *Top Left*: Timelapse of GCaMP6s signal (green) and H2B-mCherry (magenta) from 200 frame (11 min 28 s) recording of skin capillary ECs from wildtype (WT) mice prior to DMSO treatment, imaged at a frame rate of 3.441s/frame (scale bar: 20 µm). *Top Right*: Timelapse of revisited region after DMSO treatment. *Bottom Left*: Timelapse of ECs prior to nifedipine treatment. *Bottom Right*:

Timelapse of revisited region after nifedipine treatment. All timelapses are followed by max intensity projection of GCaMP6s signal represented with fire lookup table. Color scale indicates GCaMP6s signal over recording time.

Movie 7 L-type VGCC inhibition decreases EC Ca^{2+} activity after Cx43cKO *Top Left*: Timelapse of GCaMP6s signal (green) and H2B-mCherry (magenta) from 200 frame (11 min 28 s) recording of skin capillary ECs from Cx43cKO mice prior to DMSO treatment, imaged at a frame rate of 3.441s/frame (scale bar: 20 µm). *Top Right*: Timelapse of revisited region after DMSO treatment. *Bottom Left*: Timelapse of ECs prior to nifedipine treatment. *Bottom Right*: Timelapse of revisited region after nifedipine treatment. All timelapses are followed by max intensity projection of GCaMP6s signal represented with fire lookup table. Color scale indicates GCaMP6s signal over recording time.

References

1. A. A. Domenighetti, J. L. Beny, F. Chabaud, M. Frieden, An intercellular regenerative calcium wave in porcine coronary artery endothelial cells in primary culture. *J Physiol* **513 (Pt 1)**, 103-116 (1998).
2. W. N. Ross, Understanding calcium waves and sparks in central neurons. *Nat Rev Neurosci* **13**, 157-168 (2012).
3. R. Balaji *et al.*, Calcium spikes, waves and oscillations in a large, patterned epithelial tissue. *Sci Rep* **7**, 42786 (2017).
4. J. L. Moore *et al.*, Cell cycle controls long-range calcium signaling in the regenerating epidermis. *J Cell Biol* **222** (2023).
5. S. B. David, K. Y. L. Ho, G. Tanentzapf, A. Zaritsky, Formation of recurring transient Ca(2+)-based intercellular communities during Drosophila hematopoiesis. *Proc Natl Acad Sci U S A* **121**, e2318155121 (2024).
6. R. E. Dolmetsch, R. S. Lewis, C. C. Goodnow, J. I. Healy, Differential activation of transcription factors induced by Ca2+ response amplitude and duration. *Nature* **386**, 855-858 (1997).
7. R. E. Dolmetsch, K. Xu, R. S. Lewis, Calcium oscillations increase the efficiency and specificity of gene expression. *Nature* **392**, 933-936 (1998).
8. P. De Koninck, H. Schulman, Sensitivity of CaM kinase II to the frequency of Ca2+ oscillations. *Science* **279**, 227-230 (1998).
9. R. Wollman, T. Meyer, Coordinated oscillations in cortical actin and Ca2+ correlate with cycles of vesicle secretion. *Nat Cell Biol* **14**, 1261-1269 (2012).
10. C. T. Berry, M. J. May, B. D. Freedman, STIM- and Orai-mediated calcium entry controls NF-kappaB activity and function in lymphocytes. *Cell Calcium* **74**, 131-143 (2018).
11. B. Debir, C. Meaney, M. Kohandel, M. B. Unlu, The role of calcium oscillations in the phenotype selection in endothelial cells. *Sci Rep* **11**, 23781 (2021).
12. B. F. Grewe *et al.*, Neural ensemble dynamics underlying a long-term associative memory. *Nature* **543**, 670-675 (2017).
13. S. P. Herbert, D. Y. Stainier, Molecular control of endothelial cell behaviour during blood vessel morphogenesis. *Nat Rev Mol Cell Biol* **12**, 551-564 (2011).
14. S. K. Sonkusare *et al.*, Elementary Ca2+ signals through endothelial TRPV4 channels regulate vascular function. *Science* **336**, 597-601 (2012).
15. E. E. Friedrich *et al.*, Endothelial cell Piezo1 mediates pressure-induced lung vascular hyperpermeability via disruption of adherens junctions. *Proc Natl Acad Sci U S A* **116**, 12980-12985 (2019).
16. P. J. Dalal, W. A. Muller, D. P. Sullivan, Endothelial Cell Calcium Signaling during Barrier Function and Inflammation. *Am J Pathol* **190**, 535-542 (2020).

17. T. A. Longden *et al.*, Local IP(3) receptor-mediated Ca(2+) signals compound to direct blood flow in brain capillaries. *Sci Adv* **7** (2021).
18. S. G. Hong *et al.*, Mechanosensitive membrane domains regulate calcium entry in arterial endothelial cells to protect against inflammation. *J Clin Invest* **134** (2024).
19. J. J. Mack *et al.*, NOTCH1 is a mechanosensor in adult arteries. *Nat Commun* **8**, 1620 (2017).
20. T. T. Liu *et al.*, Piezo1-Mediated Ca(2+) Activities Regulate Brain Vascular Pathfinding during Development. *Neuron* **108**, 180-192 e185 (2020).
21. T. A. Longden *et al.*, Capillary K(+)-sensing initiates retrograde hyperpolarization to increase local cerebral blood flow. *Nat Neurosci* **20**, 717-726 (2017).
22. O. F. Harraz, T. A. Longden, D. Hill-Eubanks, M. T. Nelson, PIP(2) depletion promotes TRPV4 channel activity in mouse brain capillary endothelial cells. *Elife* **7** (2018).
23. P. Thakore *et al.*, Brain endothelial cell TRPA1 channels initiate neurovascular coupling. *Elife* **10** (2021).
24. A. Mughal *et al.*, Electrocalcium coupling in brain capillaries: Rapidly traveling electrical signals ignite local calcium signals. *Proc Natl Acad Sci U S A* **121**, e2415047121 (2024).
25. D. C. G. Garcia, T. A. Longden, Ion channels in capillary endothelium. *Curr Top Membr* **85**, 261-300 (2020).
26. Y. N. Tallini *et al.*, Propagated endothelial Ca2+ waves and arteriolar dilation in vivo: measurements in Cx40BAC GCaMP2 transgenic mice. *Circ Res* **101**, 1300-1309 (2007).
27. I. Toma *et al.*, Connexin 40 and ATP-dependent intercellular calcium wave in renal glomerular endothelial cells. *Am J Physiol Regul Integr Comp Physiol* **294**, R1769-1776 (2008).
28. J. Sun, J. B. Hoying, P. A. Deymier, D. D. Zhang, P. K. Wong, Cellular Architecture Regulates Collective Calcium Signaling and Cell Contractility. *PLoS Comput Biol* **12**, e1004955 (2016).
29. W. F. Jackson, Endothelial Ion Channels and Cell-Cell Communication in the Microcirculation. *Front Physiol* **13**, 805149 (2022).
30. M. D. Lee *et al.*, Small-world connectivity dictates collective endothelial cell signaling. *Proc Natl Acad Sci U S A* **119**, e2118927119 (2022).
31. L. Leybaert, M. J. Sanderson, Intercellular Ca(2+) waves: mechanisms and function. *Physiol Rev* **92**, 1359-1392 (2012).
32. G. Mese, G. Richard, T. W. White, Gap junctions: basic structure and function. *J Invest Dermatol* **127**, 2516-2524 (2007).
33. C. Y. Kam *et al.*, Desmoplakin maintains gap junctions by inhibiting Ras/MAPK and lysosomal degradation of connexin-43. *J Cell Biol* **217**, 3219-3235 (2018).
34. B. R. Kwak, M. S. Pepper, D. B. Gros, P. Meda, Inhibition of endothelial wound repair by dominant negative connexin inhibitors. *Mol Biol Cell* **12**, 831-845 (2001).
35. Y. Yokota *et al.*, Endothelial Ca 2+ oscillations reflect VEGFR signaling-regulated angiogenic capacity in vivo. *Elife* **4** (2015).
36. C. Y. Kam *et al.*, Mechanisms of skin vascular maturation and maintenance captured by longitudinal imaging of live mice. *Cell* **186**, 2345-2360 e2316 (2023).
37. M. W. Sedovy *et al.*, Injury Induced Connexin 43 Expression Regulates Endothelial Wound Healing. *bioRxiv* 10.1101/2025.02.24.639946 (2025).
38. P. Quijada *et al.*, Coordination of endothelial cell positioning and fate specification by the epicardium. *Nat Commun* **12**, 4155 (2021).
39. K. Y. L. Ho, R. J. Khadilkar, R. L. Carr, G. Tanentzapf, A gap-junction-mediated, calcium-signaling network controls blood progenitor fate decisions in hematopoiesis. *Curr Biol* **31**, 4697-4712 e4696 (2021).
40. G. Bazzoni, E. Dejana, Endothelial cell-to-cell junctions: molecular organization and role in vascular homeostasis. *Physiol Rev* **84**, 869-901 (2004).
41. X. F. Figueroa, B. R. Duling, Gap junctions in the control of vascular function. *Antioxid Redox Signal* **11**, 251-266 (2009).
42. T. Krolak *et al.*, Brain endothelial gap junction coupling enables rapid vasodilation propagation during neurovascular coupling. *Cell* 10.1016/j.cell.2025.06.030 (2025).
43. M. Vanlandewijck *et al.*, A molecular atlas of cell types and zonation in the brain vasculature. *Nature* **554**, 475-480 (2018).
44. S. Joost *et al.*, The Molecular Anatomy of Mouse Skin during Hair Growth and Rest. *Cell Stem Cell* **26**, 441-457 e447 (2020).
45. E. L. Evans *et al.*, Yoda1 analogue (Dooku1) which antagonizes Yoda1-evoked activation of Piezo1 and aortic relaxation. *Br J Pharmacol* **175**, 1744-1759 (2018).

46. T. D. Helton, W. Xu, D. Lipscombe, Neuronal L-type calcium channels open quickly and are inhibited slowly. *J Neurosci* **25**, 10247-10251 (2005).
47. D. Lipscombe, T. D. Helton, W. Xu, L-type calcium channels: the low down. *J Neurophysiol* **92**, 2633-2641 (2004).
48. T. Godfraind, Discovery and Development of Calcium Channel Blockers. *Front Pharmacol* **8**, 286 (2017).
49. Y. Zhao *et al.*, Molecular Basis for Ligand Modulation of a Mammalian Voltage-Gated Ca(2+) Channel. *Cell* **177**, 1495-1506 e1412 (2019).
50. J. G. McCarron, M. D. Lee, C. Wilson, The Endothelium Solves Problems That Endothelial Cells Do Not Know Exist. *Trends Pharmacol Sci* **38**, 322-338 (2017).
51. S. S. Oladipupo *et al.*, Endothelial cell FGF signaling is required for injury response but not for vascular homeostasis. *Proc Natl Acad Sci U S A* **111**, 13379-13384 (2014).
52. L. Lamalice, F. Le Boeuf, J. Huot, Endothelial cell migration during angiogenesis. *Circ Res* **100**, 782-794 (2007).
53. L. Yuan *et al.*, A role of stochastic phenotype switching in generating mosaic endothelial cell heterogeneity. *Nat Commun* **7**, 10160 (2016).
54. N. Honkura *et al.*, Intravital imaging-based analysis tools for vessel identification and assessment of concurrent dynamic vascular events. *Nat Commun* **9**, 2746 (2018).
55. M. Richards *et al.*, Intra-vessel heterogeneity establishes enhanced sites of macromolecular leakage downstream of laminin alpha5. *Cell Rep* **35**, 109268 (2021).
56. E. Trimm, K. Red-Horse, Vascular endothelial cell development and diversity. *Nat Rev Cardiol* **20**, 197-210 (2023).
57. J. M. Gomez-Salinero, D. Redmond, S. Rafii, Microenvironmental determinants of endothelial cell heterogeneity. *Nat Rev Mol Cell Biol* **26**, 476-495 (2025).
58. A. Jambusaria *et al.*, Endothelial heterogeneity across distinct vascular beds during homeostasis and inflammation. *Elife* **9** (2020).
59. A. C. A. Cleuren *et al.*, The in vivo endothelial cell translatome is highly heterogeneous across vascular beds. *Proc Natl Acad Sci U S A* **116**, 23618-23624 (2019).
60. R. Marcu *et al.*, Human Organ-Specific Endothelial Cell Heterogeneity. *iScience* **4**, 20-35 (2018).
61. D. J. Nolan *et al.*, Molecular signatures of tissue-specific microvascular endothelial cell heterogeneity in organ maintenance and regeneration. *Dev Cell* **26**, 204-219 (2013).
62. C. Giorgi *et al.*, Mitochondrial Ca(2+) and apoptosis. *Cell Calcium* **52**, 36-43 (2012).
63. Y. Ladilov *et al.*, Mechanism of Ca(2+) overload in endothelial cells exposed to simulated ischemia. *Cardiovasc Res* **47**, 394-403 (2000).
64. G. Hajnoczky, E. Davies, M. Madesh, Calcium signaling and apoptosis. *Biochem Biophys Res Commun* **304**, 445-454 (2003).
65. C. Li *et al.*, SERCA overexpression reduces reperfusion-mediated cardiac microvascular damage through inhibition of the calcium/MCU/mPTP/necroptosis signaling pathways. *Redox Biol* **36**, 101659 (2020).
66. X. He *et al.*, Reduction of Mitochondria-Endoplasmic Reticulum Interactions by Acetylcholine Protects Human Umbilical Vein Endothelial Cells From Hypoxia/Reoxygenation Injury. *Arterioscler Thromb Vasc Biol* **35**, 1623-1634 (2015).
67. J. I. E. Bruce, Metabolic regulation of the PMCA: Role in cell death and survival. *Cell Calcium* **69**, 28-36 (2018).
68. P. Kameritsch, K. Pogoda, A. Ritter, S. Munzing, U. Pohl, Gap junctional communication controls the overall endothelial calcium response to vasoactive agonists. *Cardiovasc Res* **93**, 508-515 (2012).
69. A. Hautefort, A. Pfenniger, B. R. Kwak, Endothelial connexins in vascular function. *Vasc Biol* **1**, H117-H124 (2019).
70. U. Pohl, Connexins: Key Players in the Control of Vascular Plasticity and Function. *Physiol Rev* **100**, 525-572 (2020).
71. M. W. Sedovy *et al.*, Connexin 43 across the Vasculature: Gap Junctions and Beyond. *J Vasc Res* **60**, 101-113 (2023).
72. A. Zamir *et al.*, Emergence of synchronized multicellular mechanosensing from spatiotemporal integration of heterogeneous single-cell information transfer. *Cell Syst* **13**, 711-723 e717 (2022).
73. K. Parthasarathi *et al.*, Connexin 43 mediates spread of Ca2+-dependent proinflammatory responses in lung capillaries. *J Clin Invest* **116**, 2193-2200 (2006).
74. Y. Liao, K. H. Day, D. N. Damon, B. R. Duling, Endothelial cell-specific knockout of connexin 43 causes hypotension and bradycardia in mice. *Proc Natl Acad Sci U S A* **98**, 9989-9994 (2001).

75. J. L. Bossu, A. Elhamdani, A. Feltz, Voltage-dependent calcium entry in confluent bovine capillary endothelial cells. *FEBS Lett* **299**, 239-242 (1992).
76. Z. Wei, Y. Manevich, A. B. Al-Mehdi, S. Chatterjee, A. B. Fisher, Ca2+ flux through voltage-gated channels with flow cessation in pulmonary microvascular endothelial cells. *Microcirculation* **11**, 517-526 (2004).
77. M. A. Delpiano, B. M. Altura, Modulatory effect of extracellular Mg2+ ions on K+ and Ca2+ currents of capillary endothelial cells from rat brain. *FEBS Lett* **394**, 335-339 (1996).
78. M. A. Yakubu, C. W. Leffler, L-type voltage-dependent Ca2+ channels in cerebral microvascular endothelial cells and ET-1 biosynthesis. *Am J Physiol Cell Physiol* **283**, C1687-1695 (2002).
79. R. D. Zuhlke, G. S. Pitt, K. Deisseroth, R. W. Tsien, H. Reuter, Calmodulin supports both inactivation and facilitation of L-type calcium channels. *Nature* **399**, 159-162 (1999).
80. A. Hudmon *et al.*, CaMKII tethers to L-type Ca2+ channels, establishing a local and dedicated integrator of Ca2+ signals for facilitation. *J Cell Biol* **171**, 537-547 (2005).
81. A. Blaich *et al.*, Facilitation of murine cardiac L-type Ca(v)1.2 channel is modulated by calmodulin kinase II-dependent phosphorylation of S1512 and S1570. *Proc Natl Acad Sci U S A* **107**, 10285-10289 (2010).
82. K. Maciunas, M. Snipas, T. Kraujalis, L. Kraujaliene, A. V. Panfilov, The role of the Cx43/Cx45 gap junction voltage gating on wave propagation and arrhythmogenic activity in cardiac tissue. *Sci Rep* **13**, 14863 (2023).
83. A. Revilla, M. V. Bennett, L. C. Barrio, Molecular determinants of membrane potential dependence in vertebrate gap junction channels. *Proc Natl Acad Sci U S A* **97**, 14760-14765 (2000).
84. S. R. Orth, R. Nobiling, S. Bonisch, E. Ritz, Inhibitory effect of calcium channel blockers on human mesangial cell growth: evidence for actions independent of L-type Ca2+ channels. *Kidney Int* **49**, 868-879 (1996).
85. R. Berkels *et al.*, Nifedipine increases endothelial nitric oxide bioavailability by antioxidative mechanisms. *Hypertension* **37**, 240-245 (2001).
86. S. Miura, M. Fujino, Y. Matsuo, H. Tanigawa, K. Saku, Nifedipine-induced vascular endothelial growth factor secretion from coronary smooth muscle cells promotes endothelial tube formation via the kinase insert domain-containing receptor/fetal liver kinase-1/NO pathway. *Hypertens Res* **28**, 147-153 (2005).
87. M. Hirasawa, Q. J. Pittman, Nifedipine facilitates neurotransmitter release independently of calcium channels. *Proc Natl Acad Sci U S A* **100**, 6139-6144 (2003).
88. N. Korte *et al.*, The Ca2+-gated channel TMEM16A amplifies capillary pericyte contraction and reduces cerebral blood flow after ischemia. *J Clin Invest* **132** (2022).
89. N. Korte *et al.*, Inhibiting Ca(2+) channels in Alzheimer's disease model mice relaxes pericytes, improves cerebral blood flow and reduces immune cell stalling and hypoxia. *Nat Neurosci* **27**, 2086-2100 (2024).
90. H. R. Ferris *et al.*, Increased luminal pressure in brain capillaries drives TRPC3-dependent depolarization and constriction of transitional pericytes. *Sci Signal* **18**, eads1903 (2025).
91. Y. Wei *et al.*, Structural bases of inhibitory mechanism of Ca(V)1.2 channel inhibitors. *Nat Commun* **15**, 2772 (2024).
92. H. M. Nguyen *et al.*, Structural Insights into the Atomistic Mechanisms of Action of Small Molecule Inhibitors Targeting the KCa3.1 Channel Pore. *Mol Pharmacol* **91**, 392-402 (2017).
93. I. Sorensen, R. H. Adams, A. Gossler, DLL1-mediated Notch activation regulates endothelial identity in mouse fetal arteries. *Blood* **113**, 5680-5688 (2009).
94. M. R. Calera *et al.*, Connexin43 is required for production of the aqueous humor in the murine eye. *J Cell Sci* **119**, 4510-4519 (2006).
95. L. Madisen *et al.*, Transgenic mice for intersectional targeting of neural sensors and effectors with high specificity and performance. *Neuron* **85**, 942-958 (2015).
96. S. P. Peron, J. Freeman, V. Iyer, C. Guo, K. Svoboda, A Cellular Resolution Map of Barrel Cortex Activity during Tactile Behavior. *Neuron* **86**, 783-799 (2015).
97. C. M. Pineda *et al.*, Intravital imaging of hair follicle regeneration in the mouse. *Nat Protoc* **10**, 1116-1130 (2015).